Real-time Exploration and Photorealistic Reconstruction of Large Natural Environments

Nikos Komodakis and Georgios Tziritas
Computer Science Department, University of Crete
E-mails: {komod, tziritas}@csd.uoc.gr

Abstract

This paper presents a hybrid (geometry- & image-based) framework suitable for providing photorealistic walkthroughs of large, complex outdoor scenes, based only on a small set of real images from the scene. To this end, a novel data representation of a 3D scene is proposed, which is called *morphable 3D-mosaics*. Motion is assumed to be taking place along a predefined path of the 3D environment and the input to the system is a sparse set of stereoscopic views at certain positions (key-positions) along that path (one view per position). An approximate local 3D model is constructed from each view, capable of capturing the photometric and geometric properties of the scene only locally. Then during the rendering process, a continuous morphing (both photometric as well as geometric) takes place between successive local 3D models, using what we call a "morphable 3D-model". For the estimation of the photometric morphing, a robust algorithm capable of extracting a dense field of 2D correspondences between wide-baseline images is used, whereas for the geometric morphing, a novel method of computing 3D correspondences between local models is proposed. This way, a physically-valid morphing is always produced, which is thus kept transparent from the user. Moreover, a highly optimized rendering path is being used during morphing, which thus allows for high frame rates.

Our system can be extended to handle multiple stereoscopic views (and therefore multiple local models) per key-position of the path (related by a camera rotation). In this case, one local 3D-mosaic (per key-position) is constructed, comprising all local 3D models therein, and so a "morphable 3D-mosaic" is now used during the rendering process. For handling the geometric consistency of each 3D-mosaic, a technique which is based on solving a partial differential equation is adopted. The effectiveness of our framework is demonstrated by using it for the 3D visual reconstruction of the Samaria Gorge in Crete.

I. Introduction

One research problem of computer graphics that has attracted a lot of attention over the last years is the creation of modeling and rendering systems capable to provide photorealistic & interactive

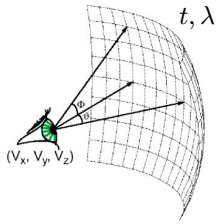

Fig. 1: A schematic view of the plenoptic function

walkthroughs of complex, real-world environments. Two are the main approaches that have been proposed so far for that purpose. On one hand, there exist those techniques that are geometry-based. These work by first trying to estimate an accurate global 3D model of the scene. They then use the extracted 3D model in order to render the scene under any given viewpoint. One of their advantages is that they provide great flexibility and allow many of the scene's properties to be modified during rendering. E.g. by having a global 3D model one can readily alter not only the viewpoint but also the lighting conditions of the scene. However, their big disadvantage comes from the fact that extracting an accurate global 3D model can be either extremely time consuming or very difficult (not to say impossible) in many cases. For example such a 3D-model construction task can be easy for scenes containing mostly planar objects (e.g. architectural-type scenes) but becomes extremely hard for outdoor scenes containing objects with irregular geometry e.g. trees. The automatic extraction of a 3D-model from images, also known as multiple view geometry, has been (and still is) an active research topic in computer vision. In fact a significant amount of progress has been achieved in this area over the last years [1]–[3].

A second class of techniques that has emerged during the last years are the so-called Image Based Rendering (IBR) methods [4]. These techniques concentrate their effort directly on how to fill the pixels of a novel view and skip the geometric modeling of the scene completely. In place of the geometric modeling, a dense set of images inside the scene is captured as a first step. One then tries to synthesize any given view by appropriately resampling the previously acquired set of captured images. By thinking of the world's appearance as a dense array of light rays filling the space, one can easily see that what all image based rendering methods actually try to do is to reconstruct the so-called *plenoptic function* [5]. This is a 7-dimensional function $P(V_x, V_y, V_z, \theta, \phi, \lambda, t)$ which models a 3D dynamic environement by recording the light rays at every space location (V_x, V_y, V_z), towards every possible direction (θ, ϕ), over any range of wavelengths λ and at any time t (see Figure 1). Each time we capture an image by a camera, the light rays passing through the camera's

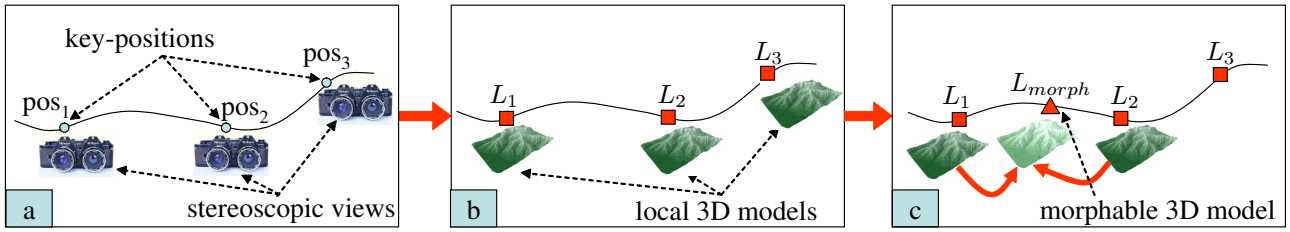

Fig. 2: (a) A sparse set of stereoscopic views is captured at key-positions along the path **(b)** One local 3D model is constructed out of each stereoscopic view **(c)** As the user traverses the path a morphable 3D model is displayed during rendering. This way, a continuous morphing between successive local models takes place at any time, with this morphing being both photometric as well as geometric.

center of projection are recorded and so that image can be considered as a specific sample of the plenoptic function. Based on these observations, image based rendering can thus be thought of as the signal processing task of *reconstructing a continuous functions (in this case the plenoptic function) based only on a discrete set of samples from that function.* As IBR methods make use of actual images from the scene under consideration, one of their greatest advantages is the fact that they can attain high levels of photorealism . However, this comes at the price of requiring a big number of captured images. This actually forms one of the biggest problem of IBR methods and is the main reason that the great majority of existing IBR techniques can be applied only to scenes of either small or medium scale. If one tries to apply such techniques to large scale scenes, then he is confronted with a huge amount of data required which makes these methods impractical for such cases.

So, while a lot of research has been done regarding small scale scenes, there are only few examples of work dealing with large scale environments. The presented framework [6], [7] is such an example of a hybrid (geometry and image based) approach, capable of providing photorealistic and interactive walkthroughs of large-scale, complex outdoor environments, using as input only a small set of images from the scene. To this end, one major contribution of this work is the proposal of a novel data representation for a 3D scene, called *morphable 3D-mosaics*, consisting of a series of morphable (both geometrically as well as photometrically) 3D models. The main assumption is that during the walkthrough, the user motion takes place along a (relatively) smooth, predefined path of the environment. The input to our system is then a sparse set of stereoscopic views captured at certain locations (which we will call *"key-positions"* hereafter) along that path (see Figure 2a). Assuming initially that only one view per key-position exists, a series of *local 3D models* are then constructed, one for each stereoscopic view, with these local models capturing the photometric and

geometric properties of the scene at a local level and containing only an approximate representation of the scene's geometry (see Figure 2b). Then, instead of trying to create a global 3D model out of all these local models (a task that can prove to be extremely difficult in many cases, requiring a very accurate registration between local models), we rather follow a different approach. The key idea is that during the transition between any two successive key-positions (say pos_1, pos_2) along the path, a *"morphable 3D-model"* L_{morph} is displayed by the rendering process (see Figure 2c). At position pos_1 this model coincides with the local model L_1 at that position, while as we are approaching pos_2 it is gradually transformed into the next local model L_2, coinciding with that upon reaching key-position pos_2. Therefore, during the rendering process, and as the user traverses the predefined path, a continuous morphing between successive local 3D models takes place all the time. It is important to note that this morphing between local models is both photometric as well as geometric. Moreover, we ensure that it always proceeds in a physically-valid way, thus remaining transparent to the user of the system. For this purpose, algorithms capable of extracting both 2D correspondences between wide-baseline images as well as 3D correspondences between local geometric models are proposed and used.

Our system can be also extended to handle the existence of multiple stereoscopic views per key position of the path, which are all related by a pure rotation of the stereoscopic camera. In that case, there will also be multiple local models per key-position. Therefore, before applying the morphing procedure, a *3D-mosaic* per key-position needs to be constructed as well. Each 3D-mosaic will simply comprise the multiple local models at the corresponding key-position and will itself be a bigger local model covering a wider field of view. Morphing can then proceed in the same way as before with the only difference being that these 3D-mosaics will be the new local 3D models to be used during the stage of morphing (in place of the smaller individual ones). So, during morphing, instead of a morphable 3D model we will now have a *morphable 3D mosaic*.

Besides the proposal of a novel hybrid representation for a 3D scene, our system also includes new algorithms and techniques as part of its image-based modeling and rendering pipeline:

- More specifically, in the context of our photometric morphing procedure, a robust method for obtaining a dense field of 2D correspondences between a pair of wide-baseline images is proposed. In this case, the problem is that, due to the wide baseline, objects in the two images may appear at different scales. Therefore, simple similarity measures (e.g. correlation), that are typically used in stereo matching, are not appropriate anymore. To deal with this issue, we first reduce this task to a discrete energy minimization problem and then, to account for the

existence of a wide baseline, the change of scale between corresponding local patches of the two images is also taken into account during the matching process (see section VI-A).

- As part of our geometric morphing procedure, 3D correspondences between local geometric models needs to be established as well. A new approach is thus proposed for that purpose. Our method is not computationally demanding and is based just on solving a standard partial differential equation (see section VI-B).
- Furthermore, in the context of the 3D mosaics construction, a technique for combining local 3D models (related to each other by a 3D rotation) is presented, which is again based on solving a standard partial differential equation. Our method is robust enough so that it can cope with errors in the geometry of the local 3D models and always ensures that a consistent 3D mosaic is generated. To this end, geometric rectifications are applied to each one of the local 3D models during their merging (see section VIII).
- Finally, as part of our rendering pipeline, we propose the use of modern graphics hardware to perform both the photometric as well as the geometric morphing, thus drastically reducing the rendering time and achieving very high frame rates (see section VII).

All of these algorithms are nicely integrated into a single framework, so that a complete, as well as powerful, image based modeling and rendering system is obtained in the end. Regarding the advantages of this system, the following points can then be made:

- To start with, no global 3D model of the environment needs to be assembled, a process which can be extremely cumbersome and error-prone for large scale scenes. For instance, the global registration of multiple local models (which is needed for creating a global 3D model) can accumulate a great amount of error, especially if the number of local models is large. In addition to that, global registration also presumes a very accurate extraction of the underlying geometry of these local models, a task which may be difficult to achieve for complex natural scenes. On the contrary, neither such an accurate geometric reconstruction of the individual local 3D models nor a very precise registration between them is required by our framework for producing satisfactory results. Furthermore, no accumulation of registration error exists in our case.
- On the other hand, by making use of an image-based data representation, our framework is also capable of fully reproducing the photorealistic richness of the scene.
- At the same time, it offers scalability to large scale environments, as only one “morphable 3D-model” is displayed at any time, while it also makes use of a rendering path which is highly optimized in modern 3D graphics hardware.

- Data acquisition is very easy (e.g. collecting the stereoscopic images for a path over 100 meters long took us only about 20 minutes) and requires no special or expensive equipment (just a pair of digital cameras and a tripod)
- Finally, our framework makes up an end-to-end system, thus providing an almost automated processing of the input data, which are just a sparse set of stereoscopic images from the scene.

II. Related work

Many examples of geometry-based modeling methods of real world scenes appear in the computer vision literature [8]–[10]. One early example, that makes use of stereoscopic image sequences, is the work of Koch [11]. Another characteristic example is the work of Pollefey et al. [12] on 3D reconstruction from hand-held cameras. Recently, multi-view 3D reconstruction methods have been proposed as well, which are either probabilistic [13] or based on PDEs (partial differential equations) [14], [15]. Also, Debevec et al. [16] have proposed a hybrid (geometry- and image-based) approach which makes use of view dependent texture mapping. However, their work is mostly suitable for architectural type scenes. Furthermore, they also assume that a basic geometric model of the whole scene can be recovered interactively. In [17], an image-based technique is proposed by which an end-user can create walkthroughs from a sequence of photographs, while in "plenoptic modeling" [18] a warp operation is introduced that maps panoramic images (along with disparity) to any desired view. However, this operation is not very suitable for use in modern 3D graphics hardware. Lightfield [19] and Lumigraph [20] are two popular image-based rendering methods but they require a large number of input images and so they are mainly used for small scale scenes.

To address this issue work on unstructured/sparse lumigraphs has been proposed by various authors. One such example is the work of Buehler et al. [21]. However, in that work, a fixed geometric proxy (which is supposed to describe the global geometry of the scene at any time instance) is being assumed, an assumption that is not adequate for the case of 3D data coming from a sequence of sparse stereoscopic views. This is in contrast to our work where view-dependent geometry is being used due to the continuous geometric morphing that is taking place. Another example of a sparse lumigraph is the work of Schirmacher et al. [22]. Although they allow the use of multiple depth maps, any possible inconsistencies between them are not taken into account during rendering. This is again in contrast to our work where an optical flow between wide-baseline images is estimated to deal with this issue. Furthermore, this estimation of optical flow between wide baseline images reduces the required number of views. For these reasons if any of the above

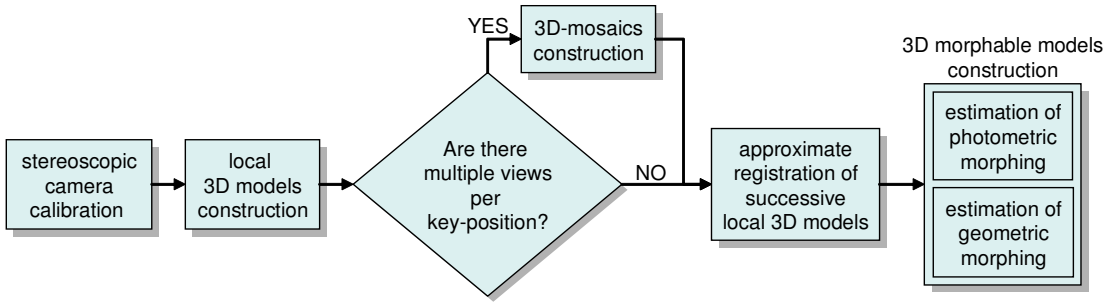

Fig. 3: The modeling pipeline

two approaches were to be applied to large-scale scenes like those handled in our case, many more images (than ours) would then be needed. Also, due to our rendering path which can be highly optimized in modern graphics hardware, we can achieve very high frame rates during rendering while the corresponding frame rates listed in [22] are necessarily low due to an expensive barycentric coordinate computation which increases the rendering time.

In [23] Vedula et al. make use of a geometric morphing procedure as well, but it is used for a different purpose, which is the recovery of the continuous 3D motion of a non-rigid dynamic event (e.g. human motion). Their method (like some other methods [24], [25]) uses multiple synchronized video streams combined with IBR techniques to render a dynamic scene, but all of these approaches are mostly suitable for scenes of smaller scale (than the ones we are interested in) since they assume that all of the cameras are static. Also, in the "Interactive visual tours" approach [26], video (from multiple cameras) is being recorded as one moves along predefined paths inside a real world environment and then image based rendering techniques are used for replaying the tour and allowing the user to move along those paths. This way, virtual walkthroughs of large scenes can be generated. Finally, in the "sea of images" approach [27], a set of omnidirectional images are captured for creating interactive walkthroughs of large, indoor environments. However, this set of images is very dense with the image spacing being $\approx$ 1.5 inches.

III. Overview of the modeling pipeline

A diagram of our system's modeling pipeline is shown in Figure 3. We will first consider the simpler case of having only one stereoscopic view per key-position of the path.

Prior to capturing these stereoscopic views, a calibration of the stereoscopic camera needs to take place first. During this stage both the external parameters (i.e. the relative 3D rotation and translation between the left and right camera) as well as the internal parameters of the stereoscopic

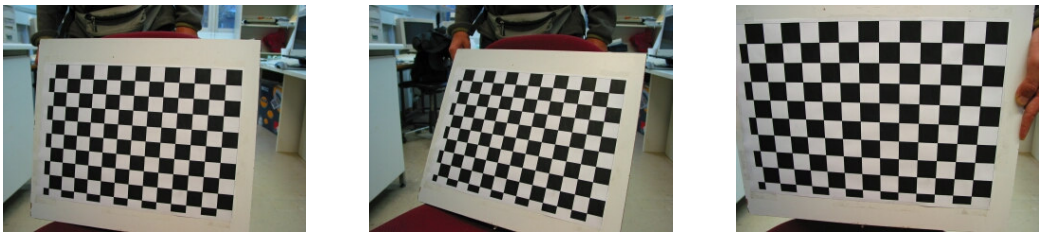

Fig. 4: For calibrating our camera we capture images of a chess pattern at random positions and orientations.

camera are estimated. We make the common assumption that both the left and right camera are modeled by the usual pinhole. In this case their internal parameters are contained in the so-called intrinsic matrices K_{left}, K_{right}. Any such matrix has the following form:

$$\begin{bmatrix} f_x & c & u_0 \\ 0 & f_y & v_0 \\ 0 & 0 & 1 \end{bmatrix}$$

where (f_x, f_y) represents the focal length, c describes the skewness of the two image axes while (u_0, v_0) represents the principal point. We also model (both radial and tangential) lens distortion and the following model is assumed for this purpose:

$$\begin{bmatrix} \hat{x} \\ \hat{y} \end{bmatrix} = \begin{bmatrix} 1 + d_1 r^2 + d_2 r^4 + d_5 r^6 + 2 d_3 xy + d_4 (r^2 + 2x^2) \\ 1 + d_1 r^2 + d_2 r^4 + d_5 r^6 + d_3 (r^2 + 2y^2) + 2 d_4 xy \end{bmatrix}$$

where (x, y) are the ideal (distortion-free) pixel coordinates, $(\hat{x}, \hat{y})$ are the corresponding observed image coordinates and $r = \sqrt{x^2 + y^2}$. For estimating all of these parameters we apply a method similar to that in [28], using as input stereoscopic image pairs of a calibrated chess pattern captured at random positions and orientations by our camera (see Figure 4).

After the camera calibration has finished, then the following stages of the modeling pipeline need to take place:

1) *Local 3D models construction (section IV):* A photometric and geometric representation of the scene near each key-position of the path is constructed. The geometric part of a local model needs to be only an approximation of the true scene geometry.
2) *Approximate registration between successive local 3D models (section V):* An estimation of the relative pose between successive local models takes place here. We should note that only a coarse estimate of the relative pose is needed, since this will not be used for an exact

(a) (b)

Fig. 5: (a) Depth map Z_0 of a local model (black pixels do not belong to its valid region dom_0). **(b)** A rendered view of the local model using an underlying triangle mesh

registration of the local models, but merely for the morphing procedure that takes place later.

3) *3D morphable models construction (section VI):* The photometric as well as the geometric morphing between successive local 3D models is estimated during this stage of the modeling pipeline.

In the case that there are multiple views per key position of the path, then, as already explained, there will also have to be an additional stage responsible for the *3D-mosaics construction*. This stage needs to take place prior to the registration step and is described in section VIII. Finally, we describe the rendering pipeline of our system in section VII.

IV. Local 3D models construction

For each stereoscopic image pair, a 3D model describing the scene locally (i.e. as seen from the camera viewpoint) must be produced during this stage. To this end, a stereo matching procedure is applied to the left and right images (denoted I_{left} and I_{right}), so that disparity can be estimated for all points inside a selected image region dom_0 of I_{left} (see section IV-A about how this disparity can be estimated). Using then the resulting disparity map (as well as the calibration matrices of the cameras) a 3D reconstruction takes place and thus the maps X_0, Y_0 and Z_0 are produced (see Fig. 5(a)). These maps respectively contain the x, y and z coordinates of the reconstructed points with respect to the 3D coordinate system of the left camera.

The set $L_0 = (X_0, Y_0, Z_0, I_{left}, dom_0)$ consisting of the images X_0, Y_0, Z_0 (the geometric-maps), the image region dom_0 (valid domain of geometric-maps) and the image I_{left} (the photometric map) makes up what we call a *"local model"* L_0. Hereafter that term will implicitly refer to such a set of elements. By applying a 2D triangulation on the image grid of a local model, a textured 3D triangle mesh can be produced. The 3D coordinates of triangle vertices are obtained from the

underlying geometric maps while texture is obtained from I_{left} and mapped onto the mesh (see Fig. 5(b)). It should be noted that the geometric maps of a local model are expected to contain only an approximation of the scene's true geometric model.

A. Disparity estimation

Disparity estimation proceeds in two stages (see Figure 6). During the first stage, we reduce the problem of stereo matching to a discrete labeling problem, which is going to be solved through the energy optimization a 1^{st} order Markov Random Field. The nodes of the corresponding MRF are going to be the pixels of the left image, while the labels belong to a discrete set of disparities $\{0, 1, \ldots, d_{max}\}$, where d_{max} represents the maximum allowed disparity. We then seek to assign a label d_p to each node p so that the following MRF energy is minimized:

$$E(\{d_p\}) = \sum_p V_p(d_p) + \sum_{(p,q)\in\aleph} V_{pq}(d_p, d_q) \ , \tag{1}$$

where the symbol $\aleph$ denotes a set of interacting pairs of pixels on the image grid (a 4-neighborhood system is assumed).

The single node potential for assigning disparity d_p to pixel p is going to be estimated as follows:

$$V_p(d_p) = w_p \cdot |I_{right}(p - d_p) - I_{left}(p)|^2$$

The factor w_p expresses a confidence measure and is used for giving less weight to pixels that are less reliable for matching, e.g. their neighborhood in the image has uniform intensity. Its value is set equal to the following sigmoid function [29], [30]:

$$w_p = \frac{1}{1 + e^{\beta(1-\alpha\lambda_p)}} \ , \tag{2}$$

where λ_p represents the minimum eigenvalue of the following autocorrelation matrix G:

$$G = \begin{bmatrix} \sum I_x^2 & \sum I_x I_y \\ \sum I_x I_y & \sum I_y^2 \end{bmatrix}$$

Here, (I_x, I_y) represents the left image gradient, while the sums are taken over a small window around the point p in the left image. The minimum eigenvalue λ_p is a measure of the "cornerness" of point p and will be large in regions with high texture variation but will be small in uniform regions. The parameters α and β in equation (2) are set so that the weights for all points p in the input left image range between 0.5 and 1.

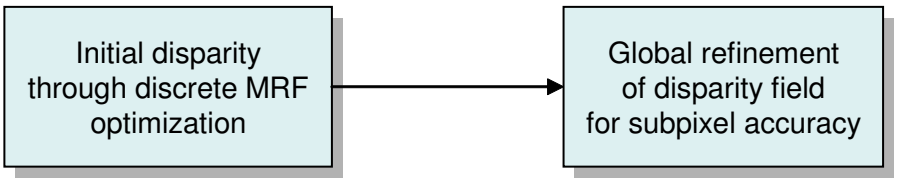

Fig. 6: The 2 stages needed for disparity estimation

Regarding the pairwise potentials of the MRF, a robust discontinuity adaptive function [31] has been chosen for them, so that a regularized solution, which also preserves discontinuities, can be computed. More specifically, the pairwise potentials have been set equal to the following truncated quadratic function, i.e.:

$$V_{pq}(d_p, d_q) = \min(\mu, |d_p - d_q|^2) \ ,$$

where μ denotes the maximum allowed penalty that can be imposed. For optimizing the energy of the above discrete MRF, the recently proposed primal-dual algorithms of Komodakis et al. [32] have been used. These methods generalize the α-expansion algorithm and can guarantee a solution which is close to the optimal one for a very wide range of pairwise potential functions.

The role of the first stage is to produce a good initial estimate of the disparity and to avoid any bad local minima during the optimization process. Its output is then given as input to the next stage of the disparity estimation process, where a global refinement of the disparity field is taking place so that a smoother field (which is more appropriate for visualizing the corresponding geometric model) is obtained in the end. For this purpose, the energy of a first order Markov Random Field is again being minimized. The difference, however, with respect to the first stage, is that now a local continuous optimization scheme is being used so that disparities with subpixel accuracy can be obtained. In particular, we use a standard gradient descent type algorithm for minimizing the same energy as in equation (1), but with the variables d_p now taking continuous values. Due to the fact that the disparity field is initialized with the result obtained from the first stage, the gradient descent algorithm usually converges very fast and does not get trapped to any poor local minima.

V. Relative pose estimation between successive local models

Let L_k=(X_k,Y_k,Z_k, I_k, dom_k) and L_{k+1}=(X_{k+1},Y_{k+1}, Z_{k+1}, I_{k+1}, dom_{k+1}) be 2 successive local models along the path. For their relative pose estimation, we need to extract a set of point matches (p_i, q_i) between the left images I_k, I_{k+1} of models L_k, L_{k+1} respectively (see section V-A). Assuming that such a set of matches already exists, then the pose estimation can proceed as follows: the 3D

points of L_k corresponding to p_i are $P_i = (X_k(p_i), Y_k(p_i), Z_k(p_i))$ and so the reprojections of p_i on image I_{k+1} are: $p'_i = K_{left}(R \cdot P_i + T) \in \mathbb{P}^2$, where R (a 3×3 orthonormal matrix) and T (a 3D vector) represent the unknown rotation and translation respectively.

So the pose estimation (i.e. the extraction of R and T) can be achieved simply by minimizing the following geometric reprojection error:

$$\sum_i dist(q_i, p'_i)^2$$

where $dist$ denotes euclidean image distance. For this purpose, an iterative constrained-minimization algorithm may be applied. During this minimization, the rotation matrix is expressed in terms of a quaternion q (i.e. a 4D-vector with $\|q\|$=1), because quaternions provide a compact representation of rotations and also exhibit no singularities (they are therefore convenient, especially for problems involving numerical optimization [33], [34]). Finally, the *essential matrix* (also computable by the help of the matches (p_i, q_i) and K_{left}, K_{right}) can be used to provide an initial estimate [1] for the iterative algorithm, so that it is not get stuck to a poor local minimum.

A. *Wide-baseline feature matching under camera looming*

Therefore the pose estimation problem is reduced to that of extracting a sparse set of correspondences between I_k, I_{k+1}. A usual method for tackling the latter problem is the following: first, a set of interest-points in I_k are extracted using an interest-point detector (e.g. the Harris corner detector). Then for each interest-point, say p, a set of candidate points CAND_p inside a large rectangular region SEARCH_p of I_{k+1} are examined and the best one is selected according to a similarity measure. Usually the candidate points are extracted by applying an interest-point detector to region SEARCH_p as well.

Unlike the left and right images of a stereoscopic view, however, the images I_k and I_{k+1} are separated by a wide baseline. Therefore, simple similarity measures for comparing image patches (e.g. correlation) have been proved extremely inefficient in such cases. Assuming a smooth predefined path (and therefore a smooth change in orientation between I_k, I_{k+1}), it is safe to assume that the main difference at an object's appearance in images I_k and I_{k+1}, comes from the forward camera motion along the Z axis (looming). The idea for extracting valid correspondences is then based on the following observation: the dominant effect of an object being closer to the camera in image I_{k+1} is that its image region in I_{k+1} appears scaled by a certain scale factor s>1. That is, if $p \in I_k, q \in I_{k+1}$ are corresponding pixels: $I_{k+1}(sq) \approx I_k(p)$. So an image patch of I_k at p should

look similar to an image patch of an appropriately rescaled (by s^{-1}) version of I_{k+1}.

Of course, the scale factor s varies across the image. Therefore the following strategy, for extracting reliable matches, can be applied:

1) Quantize the scale space of s to a discrete set of values $S = \{s_j\}_{j=0}^{n}$, where $1 = s_0 < s_1 < ... < s_n$
2) Rescale I_{k+1} by the inverse scale s_j^{-1} for all $s_j \in S$ to get rescaled images I_{k+1,s_j}
   For any $q \in I_{k+1}$, $p \in I_k$, let us denote by $\overline{I_{k+1,s_j}(q)}$ a (small) fixed-size patch around the projection of q on I_{k+1,s_j} and by $\overline{I_k(p)}$ an equal-size patch of I_k at p.
3) Given any point $p \in I_k$ and its set of candidate points $\text{CAND}_p = \{q_i\}$ in I_{k+1}, use correlation to find among the patches at any q_i and across any scale s_j, the one most similar to the patch of I_k at p:

$$(q', s') = \arg\max_{q_i, s_j} corr(\ \overline{I_{k+1,s_j}(q_i)},\ \overline{I_k(p)}\ )$$

   This way, apart from a matching point $q' \in I_{k+1}$, a scale estimate s' is provided for point p as well .

The above strategy has been used in all of the presented examples and has proved to be very effective, giving a high percentage of exact matches even in situations with very large looming. Such an example can be seen in Fig. 7 wherein the images baseline is $\approx$ 15 meters, resulting in scale factors of size ≈ 2.5 for certain image regions. Even if we set as candidate points CAND_p of a point p, all points inside SEARCH_p in the other image (and not only detected interest-points therein), the above procedure still picks the right matches in most cases. The results in Figure 8 have been produced in this way, thus showing the effectiveness of our method. Of course, more elaborate wide-baseline matching techniques can be chosen to be used at this stage as well [35]–[37].

VI. Morphing estimation between successive local models along the path

At the current stage of the modeling pipeline, a series of approximate local 3D models (along with approximate estimates of the relative pose between every successive two) are available to us. Let $L_k = (X_k, Y_k, Z_k, I_k, dom_k),\ L_{k+1} = (X_{k+1}, Y_{k+1}, Z_{k+1}, I_{k+1}, dom_{k+1})$ be such a pair of successive local models and pos_k, pos_{k+1} their corresponding key-positions on the path. By making use of the approximate pose estimate between L_k and L_{k+1}, we will assume hereafter that the 3D vertices of both models are expressed in a common 3D coordinate system.

Rather than trying to create a consistent global model by combining all local ones (a rather tedious task requiring among others high quality geometry and pose estimation) we will instead

(a) (b)

Fig. 7: (a) Image I_k along with computed optical flow vectors (blue segments) for all points marked white. **(b)** Image I_{k+1} along with matching points (also marked white) for all marked points of (a). A few epipolar lines are also shown. In both images, the yellow square around a point is proportional to the point's estimated scale factor (10 scales $S = \{1, 0.9^{-1}, ..., 0.1^{-1}\}$ have been used).

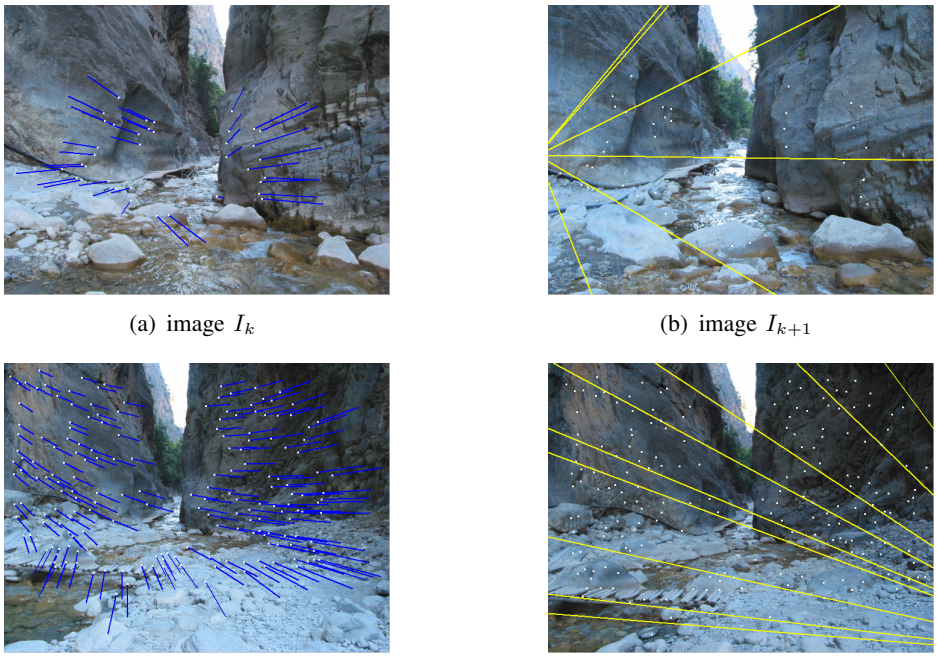

(a) image I_k (b) image I_{k+1}

(c) image I_k (d) image I_{k+1}

Fig. 8: Two more examples (one example per row) of wide baseline matching from another scene. Optical flow vectors (on image I_k) as well as estimated epipolar lines (on image I_{k+1}) are shown again. Also, notice the large camera motion taking place in the top example e.g. the stones in the water appear much closer to the camera in figure (b) than in figure (a).

follow a different approach which is based on the following observation: near path point pos_k, model L_k is ideal for representing the surrounding scene. On the other hand, as we move forward along the path approaching key-position of the next model L_{k+1}, the photometric and geometric properties of the environment are much better captured by the latter model. (For example compare the fine details of the rocks that are revealed in Fig. 7(b) and are not visible in Fig. 7(a)). So during

transition from pos_k to pos_{k+1}, we will try to gradually morph model L_k into a new destination model, which should coincide with L_{k+1} upon reaching point pos_{k+1}. (In fact, only part of this destination model can coincide with L_{k+1} since in general L_k, L_{k+1} will not represent exactly the same part of the scene). This morphing should be geometric as well as photometric (the latter wherever possible) and should proceed in a physically valid way. For this reason, we will use what we call a *"morphable 3D-model"*:

$$L_{morph} = L_k \cup (X_{dst}, Y_{dst}, Z_{dst}, I_{dst})$$

In addition to including the elements of L_k, L_{morph} also consists of maps $X_{dst}, Y_{dst}, Z_{dst}$ and map I_{dst} containing respectively the destination 3D vertices and destination color values for all points of L_k. At any time during the rendering process, the 3D coordinates $vert_{ij}$ and color col_{ij} of the vertex of L_{morph} at point (i, j) will then be:

$$vert_{ij} = \begin{bmatrix} (1-m)X_k(i,j) + mX_{dst}(i,j) \\ (1-m)Y_k(i,j) + mY_{dst}(i,j) \\ (1-m)Z_k(i,j) + mZ_{dst}(i,j) \end{bmatrix} \tag{3}$$

$$col_{ij} = (1-m)I_k(i,j) + mI_{dst}(i,j) \tag{4}$$

where m is a parameter determining the amount of morphing (m=0 at pos_k, m=1 at pos_{k+1} and $0<m<1$ in between). Specifying therefore L_{morph} amounts to filling-in the values of the destination maps $\{X, Y, Z, I\}_{dst}$ for each point $p \in dom_k$.

For this purpose, a 2-step procedure will be followed that depends on whether point p has a physically corresponding point in L_{k+1} or not:

1) Let Ψ be that subset of region $dom_k \subseteq I_k$, consisting only of those L_k points that have physically corresponding points in model L_{k+1} and let $u_{k \to k+1}$ be a function which maps these points to their counterparts in the I_{k+1} image. (Region Ψ represents that part of the scene which is common to both models L_k, L_{k+1}). Since model L_k (after morphing) should coincide with L_{k+1}, it must then hold:

$$\begin{bmatrix} X_{dst}(p) \\ Y_{dst}(p) \\ Z_{dst}(p) \\ I_{dst}(p) \end{bmatrix} = \begin{bmatrix} X_{k+1}(u_{k \to k+1}(p)) \\ Y_{k+1}(u_{k \to k+1}(p)) \\ Z_{k+1}(u_{k \to k+1}(p)) \\ I_{k+1}(u_{k \to k+1}(p)) \end{bmatrix} \quad \forall p \in \Psi \tag{5}$$

Points of region Ψ are therefore transformed both photometrically and geometrically.

2) The rest of the points (that is points in $\bar{\Psi}$=$dom_k \backslash \Psi$) do not have counterparts in model L_{k+1}. So these points will retain their color value (from model L_k) at the destination maps and no photometric morphing will take place:

$$I_{dst}(p) = I_k(p), \ \forall p \in \bar{\Psi} \tag{6}$$

But we still need to apply geometric morphing to those points so that no distortion/discontinuity in the 3D structure is observed during transition from pos_k to pos_{k+1}. Therefore we still need to fill-in the destination 3D coordinates for all points in $\bar{\Psi}$.

The 2 important remaining issues (which also constitute the core of the morphing procedure) are:

- How to compute the mapping $u_{k \to k+1}$. This is equivalent to estimating a 2D optical flow field between the left images I_k and I_{k+1}.
- And how to obtain the values of the destination geometric-maps at the points inside region $\bar{\Psi}$, needed for the geometric morphing therein.

Both of these issues will be the subject of the two subsections that follow.

A. Estimating optical flow between wide-baseline images I_k and I_{k+1}

In general, obtaining a reliable, relatively-dense optical flow field between wide-baseline images like I_k and I_{k+1} is a particularly difficult problem. Without additional input, usually only a sparse set of optical flow vectors can be obtained in the best case. In this case the basic problems are:

1) For every point in I_k, a large region of image I_{k+1} has to be searched for obtaining a corresponding point. This way the chance of an erroneous optical flow vector increases significantly (as well as the computational cost)
2) Simple measures (like correlation) are very inefficient for comparing pixel blocks between wide-baseline images
3) Even if both of the above problems are solved, optical flow estimation is inherently an ill-posed problem and additional assumptions are needed. In particular, we need to somehow impose the condition that the optical flow field will be piecewise smooth.

For dealing with the first problem, we will make use of the underlying geometric maps X_k,Y_k,Z_k of model L_k as well as the relative pose between I_k and I_{k+1}. By using these quantites, we can theoretically reproject any point, say p, of I_k onto image I_{k+1}. In practice, since all of the

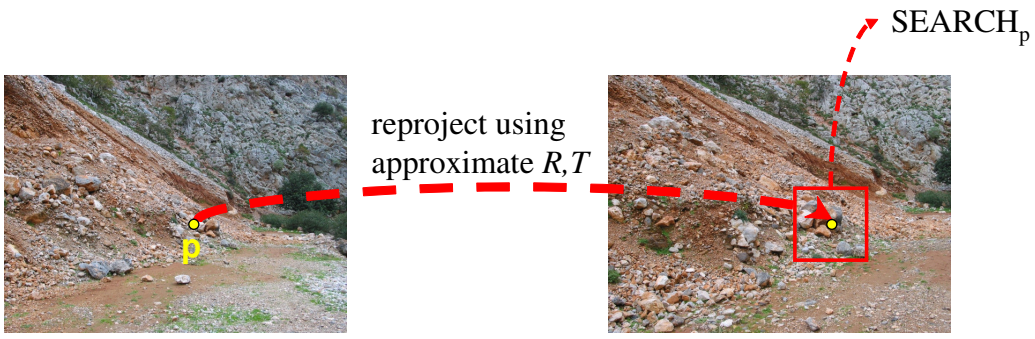

Fig. 9: Using the geometry of L_k as well as the approximate rotation R and translation T between local models L_k and L_{k+1}, any point p in image I_k is reprojected onto I_{k+1} and only a small region SEARCH$_p$ around that reprojection is searched for correspondences. We thus reduce the chance of an error as well as the overall computational cost.

above quantities are estimated only approximately, this permits us just to restrict the searching over a smaller region SEARCH$_p$ around the reprojection point (see Figure 9). The search region SEARCH$_p$ can be further restricted by taking its intersection with a small zone around the epipolar line corresponding to p. In addition, since we are interested in searching only for points of I_{k+1} that belong to dom_{k+1} (this is where L_{k+1} is defined), the final search region SEARCH$_p$ of p will be SEARCH$_p \cap dom_{k+1}$. If the final SEARCH$_p$ is empty, then no optical flow vector will be estimated and point p will be considered as not belonging to region Ψ.

For dealing with the second problem, we will use a technique similar to the one described in section V-A for getting a sparse set of correspondences. As already stated therein, the dominant effect due to a looming of the camera is that pixel neighborhoods in image I_{k+1} are scaled by a factor varying across the image. The solution proposed therein was to compare image patches of I_k not only with patches from I_{k+1} but also with patches from rescaled versions of the latter image. We will use the same technique here, with the only difference being that instead of doing that for a sparse group of features we will now apply it to a dense set of pixels of image I_k. For this purpose we will again use a discrete set of scale factors $S = \{1{=}s_0{<}s_1{<}...{<}s_n\}$ and we will rescale image I_{k+1} by each one of these factors where, as before, image I_{k+1} rescaled by s^{-1} (with $s \in S$) will be denoted by $I_{k+1,s}$. As we shall see in the next paragraph, this will have the effect of having to change the type of labels that we will use in the associated labeling problem.

Finally, to deal with the ill-posed character of the problem, we will first reduce the optical flow estimation to a discrete labeling problem and then formulate it in terms of minimizing the energy of a first order Markov Random Field [38]. What is worth noting here is that, contrary to a standard optical flow estimation procedure, the labels will now consist of vectors $l = (d_x, d_y, s) \in \mathbb{R}^2 \times S$,

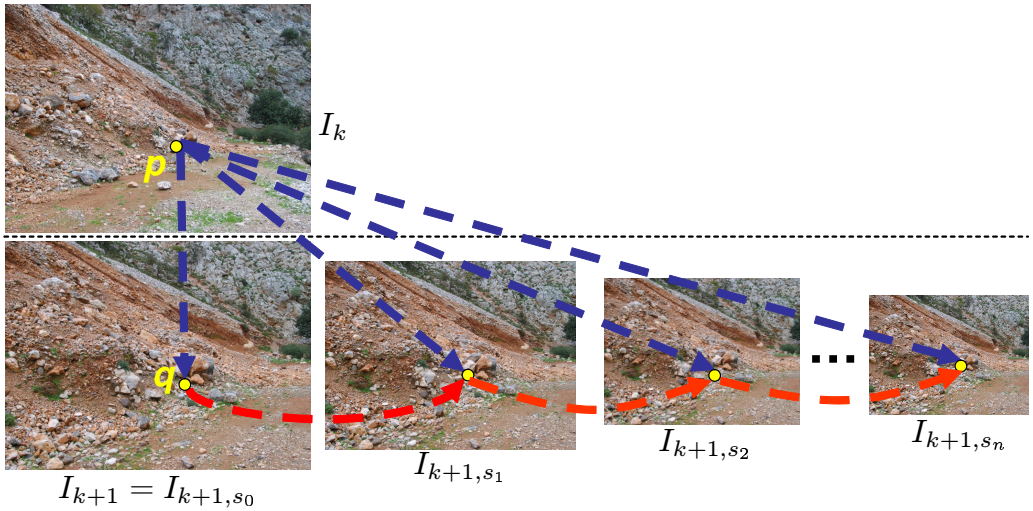

Fig. 10: Given a point $p \in I_k$ and a candidate matching point $q \in I_{k+1}$, we search across a range of scales $1{=}s_0{<}s_1{<}\ldots{<}s_n$ by first projecting q on rescaled images and then comparing the neighborhood of each of the resulting pixels with the neighborhood of p in I_k.

where the first 2 coordinates denote the components of the optical flow vector while the third one denotes the scale factor. This means that after labeling, not only an optical flow but also a scale estimation will be provided for each point (see Fig. 11(a)). Given a label l, we will denote its optical flow vector by $flow(l) = (d_x, d_y)$ and its scale by $scale(l) = s$. Based on what was already mentioned above, the labels which are allowed to be assigned to a point p in I_k will be coming from the following set: $\text{LABELS}_p = \{q - p : q \in \text{SEARCH}_p\} \times S$. This definition of the label set LABELS_p simply encodes the following two things:

- For any point p of the first image, we are searching for corresponding points q only inside the restricted region SEARCH_p
- We also search across all scales in S i.e. given a candidate matching point $q \in \text{SEARCH}_p$ for p, we compare patch $\overline{I_k(p)} \in I_k$ with any of the patches $\overline{I_{k+1,s}(q)} \in I_{k+1,s}$ where the scale s traverses all the elements of set S (see Figure 10). As before $\overline{I_k(p)}$ denotes a fixed size patch around p while $\overline{I_{k+1,s}(q)}$ denotes an equal-size patch which is located around the projection of q on the rescaled image $I_{k+1,s}$.

Getting an optical flow field is then equivalent to picking one element from the cartesian product $\text{LABELS} = \prod_{p \in \Psi} \text{LABELS}_p$. In our case, that element f of LABELS which minimizes the following energy should be chosen:

$$E(f) = \sum_{(p,p') \in \aleph} V_{p,p'}(f_p, f_{p'}) + \sum_{p \in \Psi} V_p(f_p)$$

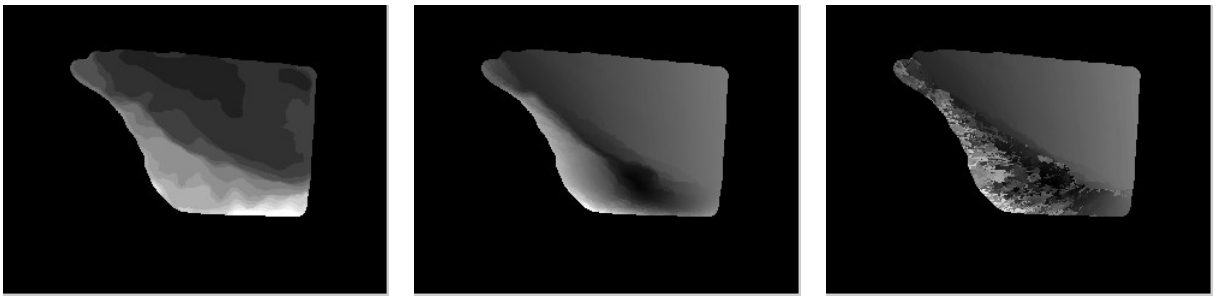

(a) (b) (c)

Fig. 11: Maps of: **(a)** *scale factors* and **(b)** *optical flow magnitudes* for all points in Ψ, as estimated after applying the optical flow algorithm to the images of Fig. 7 and while using 10 possible scales $S = \{1, 0.9^{-1}, ..., 0.1^{-1}\}$. **(c)** Corresponding optical flow magnitudes when only one scale $S = \{1\}$ has been used. As expected, in this case the algorithm fails to produce exact optical flow for points that actually have larger scale factors. We note that darker pixels in a grayscale image correspond to smaller values.

The first sum in $E(f)$ represents the prior term and penalizes optical flow fields which are not piecewise smooth, whereas the second sum in the above energy represents the likelihood and measures how well the corresponding optical flow agrees with the observed image data. The symbol $\aleph$ denotes a set of interacting pairs of pixels inside Ψ (we typically assume a 4-neighborhood system) and $V_{p,p'}(\cdot,\cdot)$ denotes the pairwise potential function of the MRF. In our case, a simple potential function that can be used is the so-called Potts function, i.e. $V_{p,p'}(f_p, f'_p)$ is equal to a non-zero constant if $f_p \neq f'_p$ and is zero otherwise. Another, more elaborate, pairwise potential function that has been also tested is the following one:

$$V_{p,p'}(f_p, f_{p'}) = \min\big(||flow(f_p) - flow(f_{p'})||^2 + |scale(f_p) - scale(f_{p'})|^2, \mu \big) \ ,$$

where μ denotes the maximum pairwise penalty that can be imposed.

Regarding the terms $V_p(f_p)$, these measure the correlation between corresponding image patches as determined by the labeling f. According to a labeling f, for a point p in I_k its corresponding point is the projection into image $I_{k+1,scale(f_p)}$ of point $p + flow(f_p)$. This means that we should compare the patches $\overline{I_k(p)}$ and $\overline{I_{k+1,scale(f_p)}(p + flow(f_p))}$ and, for this reason, we set:

$$V_p(f_p) = corr(\ \overline{I_k(p)}\ ,\ \overline{I_{k+1,scale(f_p)}(p + flow(f_p))}\ )$$

The above energy $E(f)$ can be minimized using any of the standard MRF optimization algorithms including, for example, the iterated conditional modes (ICM) algorithm [38], loopy belief propagation [39], graph-cuts [40] or any of the recently introduced primal-dual algorithms in [32]. The resulting optical flow, obtained when using the two images of Figure 7 as input, is shown in Figure

11. For comparison, we also show there (Figure 11(c)) the corresponding optical flow result which is estimated if no search across scales takes place i.e. $S = \{1\}$. As expected, in this case, the resulting optical flow is very noisy for regions that are actually undergoing a large change of scale.

B. Geometric morphing in region $\bar{\Psi}$

After estimation of optical flow $u_{k\rightarrow k+1}$, we may apply equation (5) to all points in Ψ and thus fill the arrays $X_{dst}, Y_{dst}, Z_{dst}$ therein (see Fig. 12(a)). Therefore, at this stage of the modeling pipeline, the values of the destination geometric maps $X_{dst}, Y_{dst}, Z_{dst}$ are known for all points inside region Ψ but are unknown for all points inside region $\bar{\Psi} = dom_k \backslash \Psi$ (i.e. the region which is the complement of Ψ in dom_k). Hereafter, the already known values of the destination geometric maps will be denoted by $\hat{X}_{dst}, \hat{Y}_{dst}, \hat{Z}_{dst}$ i.e. we define:

$$\hat{X}_{dst} \equiv X_{dst}|_{\Psi}, \;\; \hat{Y}_{dst} \equiv Y_{dst}|_{\Psi}, \;\; \hat{Z}_{dst} \equiv Z_{dst}|_{\Psi}$$

To completely specify morphing, we still need to fill the values of the destination geometric maps for all points in $\bar{\Psi} = dom_k \backslash \Psi$. In other words, we need to specify the destination 3D vertices for all points of L_k in $\bar{\Psi}$. Since these points do not have a physically corresponding point in L_{k+1}, we cannot apply (5) to get a destination 3D vertex from model L_{k+1}. The simplest solution would be that no geometric morphing is applied to these points and that their destination vertices just coincide with their L_k vertices. However, in that case:

- points in Ψ will have destination vertices from L_{k+1}
- while points in $\bar{\Psi}$ will have destination vertices from L_k

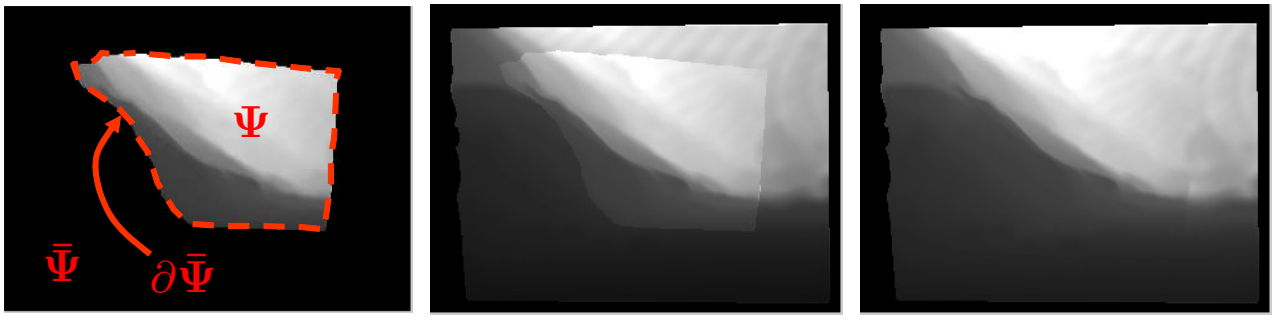

(a) (b) (c)

Fig. 12: (a) Destination depth map Z_{dst} for points inside region Ψ after using optical flow of Fig. 11(b) and applying eq. (5). To completely specify morphing we need to extend this map to the points in region $\bar{\Psi}$ **(b)** Depth map Z_{dst} of (a) extended to points in $\bar{\Psi}$ without applying geometric morphing. Notice that there exist discontinuities along the boundary $\partial\bar{\Psi}$. **(c)** Depth map Z_{dst} of (a) extended to points in $\bar{\Psi}$ after applying geometric morphing.

(a) (b) (c)

Fig. 13: Rendered views of the morphable 3D-model during transition from the key-position corresponding to image 7(a) to the key-position of image 7(b): **(a)** when no geometric morphing is applied to points in $\bar{\Psi}$ and **(b)** when geometric morphing is applied to points in $\bar{\Psi}$. **(c)** A close-up view of the rendered image in (b). Although there is no geometric discontinuity, there is a difference in texture resolution between the left part of the image (points in $\bar{\Psi}$) and the right part (points in Ψ) because only points of the latter part are morphed photometrically.

The problem resulting out of this situation is that the produced destination maps $X_{dst}, Y_{dst}, Z_{dst}$ (see Figs. 12(b), 13(a)) will contain discontinuities along the boundary (say $\partial\bar{\Psi}$) between regions Ψ and $\bar{\Psi}$, causing this way annoying discontinuity artifacts (holes) in the geometry of the "morphable 3D-model" during the morphing procedure. This will happen because the geometry of both L_k and L_{k+1} as well as their relative pose have been estimated only approximately and therefore these two models may not match perfectly when placed in a common 3D coordinate system.

The right way to fill-in the destination vertices at the points in $\bar{\Psi}$ is based on the observation that a physically valid destination 3D model should satisfy the following 2 conditions:

1) On the boundary of $\bar{\Psi}$, no discontinuity in 3D structure should exist i.e. the unknown values of $X_{dst}, Y_{dst}, Z_{dst}$ along the boundary $\partial\bar{\Psi}$ should match the corresponding known values specified by $\hat{X}_{dst}, \hat{Y}_{dst}, \hat{Z}_{dst}$ along that boundary
2) In the interior of $\bar{\Psi}$, the relative 3D structure of the initial L_k model should be preserved

Intuitively, these two conditions simply imply that, as a result of morphing, vertices of L_k inside $\bar{\Psi}$ must be deformed without distorting their relative 3D structure so as to seamlessly match the 3D vertices of L_{k+1} along the boundary of $\bar{\Psi}$. In mathematical terms the first condition obviously translates to:

$$X_{dst}|_{\partial\bar{\Psi}} = \hat{X}_{dst}|_{\partial\bar{\Psi}},\ Y_{dst}|_{\partial\bar{\Psi}} = \hat{Y}_{dst}|_{\partial\bar{\Psi}},\ Z_{dst}|_{\partial\bar{\Psi}} = \hat{Z}_{dst}|_{\partial\bar{\Psi}}$$

while the second condition, which imposes the restriction of preserving the relative 3D structure of L_k, simply implies:

$$\begin{bmatrix} X_{dst}(p) - X_{dst}(p') \\ Y_{dst}(p) - Y_{dst}(p') \\ Z_{dst}(p) - Z_{dst}(p') \end{bmatrix} = \begin{bmatrix} X_k(p) - X_k(p') \\ Y_k(p) - Y_k(p') \\ Z_k(p) - Z_k(p') \end{bmatrix}, \forall p, p' \in \bar{\Psi}$$

which is easily seen to be equivalent to:

$$\begin{bmatrix} \nabla X_{dst}(p) \\ \nabla Y_{dst}(p) \\ \nabla Z_{dst}(p) \end{bmatrix} = \begin{bmatrix} \nabla X_k(p) \\ \nabla Y_k(p) \\ \nabla Z_k(p) \end{bmatrix}, \ \forall p \in \bar{\Psi}$$

We may then extract the destination vertices by solving 3 independent minimization problems (one for each of $X_{dst}, Y_{dst}, Z_{dst}$) which are all of the same type. It therefore suffices to consider only one of them. E.g. for estimating Z_{dst} we need to find the solution to the following optimization problem:

$$\min_{Z_{dst}} \iint_{\bar{\Psi}} \|\nabla Z_{dst} - \nabla Z_k\|^2, \quad \text{with } Z_{dst}|_{\partial\bar{\Psi}} = \hat{Z}_{dst}|_{\partial\bar{\Psi}} \tag{7}$$

For discretizing the above problem we can make use of the underlying discrete pixel grid. To this end, we assume a 4-system neighborhood for the image pixels and we denote by $\mathcal{N}(p)$ the corresponding neighborhood of pixel p. In this case, the boundary $\partial\bar{\Psi}$ equals the set $\partial\bar{\Psi} = \{p \in \Psi : \mathcal{N}(p) \cap \bar{\Psi} \neq \emptyset\}$ and the finite-difference discretization of (7) yields the following quadratic optimization problem:

$$\min_{Z_{dst}} \sum_{p \in \bar{\Psi}} \sum_{q \in \mathcal{N}(p)} \big(Z_{dst}(p) - Z_{dst}(q) - [Z_k(p) - Z_k(q)]\big)^2 \ \text{ with } Z_{dst}(p) = \hat{Z}_{dst}(p), \ \forall p \in \partial\bar{\Psi} \tag{8}$$

This quadratic problem is, in turn, equivalent to the following system of linear equations:

$$|\mathcal{N}(p)| Z_{dst}(p) - \sum_{q \in \mathcal{N}(p)} Z_{dst}(q) = \sum_{q \in \mathcal{N}(p)} (Z_k(p) - Z_k(q)), \quad \forall p \in \bar{\Psi} \tag{9}$$

$$Z_{dst}(p) = \hat{Z}_{dst}(p), \quad \forall p \in \partial\bar{\Psi} \tag{10}$$

than can be solved with an iterative algorithm very efficiently due to the fact that all these linear equations form a sparse (banded) system.

Also, an alternative way of solving our optimization problem in (7) is by observing that any function minimizing (7) is also a solution to the following Poisson equation with Dirichlet boundary conditions [41], [42]:

$$\triangle Z_{dst} = \text{div}(\nabla Z_k), \quad \text{with } Z_{dst}|_{\partial\bar{\Psi}} = \hat{Z}_{dst}|_{\partial\bar{\Psi}} \tag{11}$$

```
// Vertex shader
void main()
{
 // set texture coordinates for multitexturing
 gl_TexCoord[0] = gl_MultiTexCoord0;
 gl_TexCoord[1] = gl_MultiTexCoord1;

 gl_Position = ftransform();
}

// Pixel shader
uniform float m; // the amount of morphing
uniform sampler2D tex0; //texture of image I_k
uniform smpaler2D tex1; //texture of image I_{k+1}

void main()
{
 vec2 st0 = texture2D(tex0,gl_TexCoord[0].st);
 vec2 st1 = texture2D(tex1,gl_TexCoord[1].st);
 gl_FragColor = (1-m)*st0+m*st1;
}
```

```
...

// enable vertex blending with 2 weights
glEnable(GL_VERTEX_BLEND_ARB);
glVertexBlendARB(2);
...

// set 1^st blending weight for MESH^k_Ψ, MESH^k_Ψ̄
glWeightfvARB( 1-m );

// you can now render MESH^k_Ψ, MESH^k_Ψ̄
glMatrixMode(GL_MODELVIEW0_ARB);
...

// set 2^nd blending weight for MESH^dst_Ψ, MESH^dst_Ψ̄
glWeightfvARB( m );

// you can now render MESH^dst_Ψ, MESH^dst_Ψ̄
glMatrixMode(GL_MODELVIEW1_ARB);
...
```

Fig. 14: Left: Pixel shader code (and the associated vertex shader code), written in GLSL (OpenGL Shading Language), for implementing the photometric morphing. **Right:** Skeleton code in C for applying vertex blending in OpenGL.

Therefore, in this case, in order to extract the geometric maps $X_{dst}, Y_{dst}, Z_{dst}$ it suffices that we solve 3 independent Poisson equations of the above type. See Figures 12(c), 13(b) for a result produced with this method.

VII. Rendering pipeline

An important advantage of our framework is that, regardless of the scene's size, only one "morphable 3D-model" L_{morph} needs to be displayed at any time during rendering i.e. the rendering pipeline has to execute the geometric and photometric morphing for only one local model L_k (as described in section VI). This makes our system extremely scalable to large scale scenes. In addition to that, by utilizing the enhanced capabilities of modern 3D graphics hardware, both types of morphing can admit a GPU[1] implementation, thus making our system ideal for 3D acceleration and capable of achieving very high frame rates during rendering.

More specifically, for implementing the photometric morphing of model L_k, *multitexturing* needs to be employed as a first step. To this end, both images I_k, I_{k+1} will be used as textures and each 3D vertex whose corresponding 2D point $p \in I_k$ is located inside region Ψ will be assigned 2 pairs of texture coordinates: the first pair will coincide with the image coordinates of point $p \in I_k$ while the second one will be equal to the image coordinates of the corresponding point $u_{k\to k+1}(p) \in I_{k+1}$ (see (5)). Then, given these texture coordinates, a so-called *pixel-shader* (along with its associated

[1]GPU stands for Graphics Processing Unit

vertex-shader) [43] can simply blend the two textures in order to implement (on the GPU) the photometric morphing defined by (4). Pixel and vertex shaders are user defined scripts that are executed by the GPU for each incoming 3D vertex and output pixel respectively. One possible implementation of such scripts, for the case of photometric morphing, is shown on the left side of Figure 14 where, for this specific example, the OpenGL Shading Language (GLSL) [43] has been used for describing the shaders. As for the 3D vertices which are associated to points located inside region $\bar{\Psi}$, the situation is even simpler since no actual photometric morphing takes place in there (see (6)) and so only image I_k needs to be texture-mapped onto these vertices.

On the other hand, for implementing the geometric morphing, the following procedure is used: two 2D triangulations of regions Ψ, $\bar{\Psi}$ are first generated resulting into two 2D triangle meshes $\text{TRI}_{\Psi}, \text{TRI}_{\bar{\Psi}}$. Based on these triangulations and the underlying geometric maps of L_k, two 3D triangle meshes $\text{MESH}^k_{\Psi}, \text{MESH}^k_{\bar{\Psi}}$ are constructed. Similarly, using $\text{TRI}_{\Psi}, \text{TRI}_{\bar{\Psi}}$ and the destination geometric maps $X_{dst}, Y_{dst}, Z_{dst}$, two more 3D triangle meshes $\text{MESH}^{dst}_{\Psi}, \text{MESH}^{dst}_{\bar{\Psi}}$ are constructed as well. It is then obvious that geometric morphing (as defined by (3)) amounts to a simple *vertex blending* operation i.e. meshes $\text{MESH}^k_{\Psi}, \text{MESH}^k_{\bar{\Psi}}$ are weighted by $1-m$, meshes $\text{MESH}^{dst}_{\Psi}, \text{MESH}^{dst}_{\bar{\Psi}}$ are weighted by m and the resulting weighted vertices are then added together. Vertex blending, however, is an operation that is directly supported by all modern GPUs and, as an example, Figure 14 (right box) contains skeleton code in C showing how one can implement vertex blending using the OpenGL standard.

Therefore, based on the above observations, rendering a morphable model simply amounts to feeding into the GPU just 4 textured triangle meshes. This is, however, a rendering path which is highly optimized in all modern GPUs and, therefore, a considerable amount of 3D acceleration can be achieved this way during the rendering process.

A. Decimation of local 3D models

Up to now we have assumed that a full local 3D model is constructed each time, i.e. all points of the image grid are included as vertices in the 2D triangulations $\text{TRI}_{\Psi}, \text{TRI}_{\bar{\Psi}}$. However, we can also use simplified versions of these 2D triangle meshes, provided, of course, that these simplified meshes approximate well the underlying geometric maps [44]. In fact, due to our framework's structure, a great amount of simplification can be achieved and the reason is that a simplified model L'_k has to be a good approximation to the full local model L_k only in the vicinity of pos_k (remember that model L_k is being used only in a local region around pos_k). Based on this observation, the

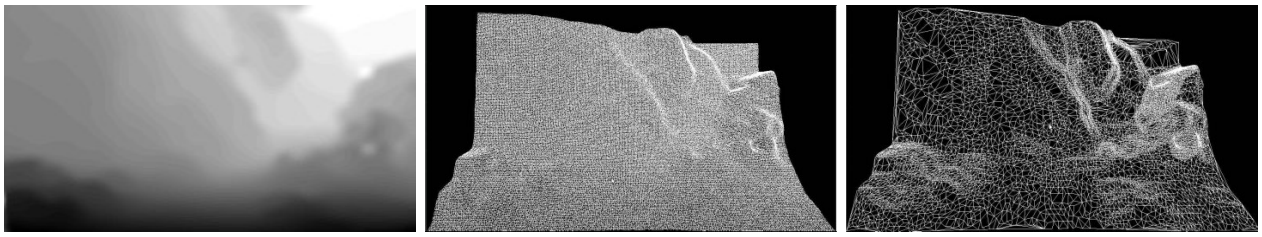

(a) (b) (c)

Fig. 15: (a) Estimated disparity field corresponding to a local 3D model L_k. **(b)** Resulting full 3D model produced when a non-decimated 2D triangulation of the geometric maps has been used. **(c)** Simplified 3D model of L_k produced using a decimated 2D triangulation where the e_{max} threshold has been set equal to 0.5 pixels.

following iterative procedure is being used for the simplification of the 2D meshes: at the start of each iteration there exists a current 2D Delaunay triangulation TRI_i which has as vertices only a subset of the points on the image grid. Based on TRI_i, an error function $e(p)$ is defined over the image grid which is measuring how well the current MESH_i approximates the underlying geometric maps (here MESH_i denotes the 3D surface defined by TRI_i). To each triangle, say T, of TRI_i we then associate the following two quantities: $e(T) = \max_{p \in T} e(p)$ (i.e. the maximum error across T) and $p(T) = \arg\max_{p \in T} e(p)$ (i.e. the interior point of T achieving this maximum error). At each iteration the triangle $T_{max} = \arg\max_{T \in \text{TRI}_i} e(T)$ of maximum error is selected and its point $p(T_{max})$ is added as a new vertex in the triangulation. This way a new Delaunay triangulation TRI_{i+1} is given as input to the next iteration of the algorithm and the process repeats until the maximum error $\max_{T \in \text{TRI}_i} e(T)$ falls below a user specified threshold e_{max}, which basically controls the total amount of simplification to be applied to the local model. Our algorithm is initialized with a sparse Delaunay triangulation TRI_0 and the only restriction imposed on TRI_0 is that it should contain the edges along the boundary between regions Ψ and $\bar{\Psi}$ (i.e. a constrained Delaunay triangulation has to be used) so that there are no cracks at the boundary of the corresponding meshes.

For completely specifying the decimation process, all that remains to be defined is the error function $e(p)$. One option would be to set $e(p) = ||\text{DEV}(p)||$ where $\text{DEV}(p) = ||\text{MESH}_i(p) - [X_k(p)\ Y_k(p)\ Z_k(p)]\,||$ denotes the geometric deviation at p between MESH_i and the underlying geometric maps ($\text{MESH}_i(p)$ is the 3D point defined by MESH_i at p). However, based on the fact that MESH_i needs to approximate L_k well only in a local region between positions pos_k and pos_{k+1} of the path, we choose to relate $e(p)$ to the maximum projection error at these locations. More specifically, we set:

$$e(p) = \max(\text{PROJ\_ERR}_{pos_k}, \text{PROJ\_ERR}_{pos_{k+1}})$$

where PROJ_ERR_{pos_k} and $\text{PROJ\_ERR}_{pos_{k+1}}$ denote the maximum projection error at positions pos_k and pos_{k+1} respectively, i.e.:

$$\text{PROJ\_ERR}_{pos_k} = \max_{p \in I_k} ||\text{PROJ}_{pos_k}(\text{DEV}(p))||$$

$$\text{PROJ\_ERR}_{pos_{k+1}} = \max_{p \in I_{k+1}} ||\text{PROJ}_{pos_{k+1}}(\text{DEV}(p))||$$

In practice this definition of the error $e(p)$ has given excellent results and managed to achieve much larger reductions in the geometric complexity of the local 3D models. Furthermore, the user-defined threshold e_{max} can now be expressed in pixel units and can thus be set in a far more intuitive way by the user. An example of a simplified local model that has been produced in this manner is shown in Figure 15, in which case e_{max} has been set equal to 0.5 pixels. We should finally note that by using the simplified local 3D models one can reduce the rendering time even further, thus achieving even higher frame rates, e.g. over 50fps.

VIII. 3D-MOSAICS CONSTRUCTION

Up to this point we have been assuming that during the image acquisition process, we have been capturing one stereoscopic image-pair per key-position along the path. We will now consider the case in which multiple stereoscopic views per key-position are captured and these stereoscopic views are related to each other by a simple rotation of the stereoscopic camera. This scenario is very useful in cases where we need to have an extended field of view (like in large VR screens) and/or when we want to be able to look around the environment. In this new case, multiple local 3D models per key-position will exist and they will be related to each other by a pure rotation in 3D space.

In order to reduce this case to the one already examined, it suffices that a single local model per key-position (called *3D-mosaic* hereafter) is constructed. This 3D model should replace all local models at that position. Then at any time during the rendering process, a morphing between a successive pair of these new local models (3D-mosaics) needs to take place as before. For this reason, the term *"morphable 3D-mosaics"* is being used in this case.

As already explained, a 3D-mosaic at a certain position along the path should replace/comprise all local models coming from captured stereoscopic views at that position. Let $L_i = (X_i, Y_i, Z_i, I_i, dom_i)$ with $i \in \{1, \ldots, n\}$ be such a set of local models. Then a new local model $L_{mosaic} = (X_{mosaic}, Y_{mosaic}, Z_{mosaic}, I_{mosaic}, dom_{mosaic})$ needs to be constructed which amounts to filling its geometric

and photometric maps. Intuitively, L_{mosaic} should correspond to a local model produced from a stereoscopic camera with a wider field of view placed at the same path position.

It is safe to assume that the images I_i (which are the left-camera images), correspond to views related to each other by a pure rotation. (Actually, the relative pose between 2 such images will not be pure rotation but will also contain a small translational part due to the fact that the stereoscopic camera rotates around the tripod and not the optical center of the left camera. However this translation is negligible in practice). We may therefore assume that the local 3D models are related to each other by a pure rotation as well. An overview of the steps that needs to be taken for the construction of L_{mosaic} now follows:

- As a first step the rotation between local models needs to be estimated. This will help us in registering the local models in 3D space.
- Then a geometric rectification of each L_i must take place so that the resulting local models are geometrically consistent with each other. This is a necessary step since the geometry of each L_i has been estimated only approximately and thus contains errors.
- Eventually, the maps of the refined and consistent local models will be merged so that the final map of the 3D-mosaic is produced

The most interesting problem that needs to be handled during the 3D-mosaic construction is that of making all models geometrically consistent so that a seamless (without discontinuities) geometric map of L_{mosaic} is produced. Each of the above steps will be explained in the following sections.

A. Rotation (R_{ij}) estimation between views I_i, I_j

First the homography H_{ij} between images I_i, I_j will be computed. (Since the views I_i, I_j are related by a rotation, H_{ij} will be the infinite homography induced by the plane at infinity.) For the H_{ij} estimation [1], a sparse set of (at least 4) point matches between I_i, I_j is first extracted and then a robust estimation procedure (e.g. RANSAC) is applied to cope with outliers. Inlier matches can then be used to refine the H_{ij} estimate by minimizing a suitable error function.

If $R_{ij} \in SO(3)$ is the 3×3 orthonormal matrix representing rotation, then: $H_{ij} = K_{left} R_{ij} K_{left}^{-1} \Leftrightarrow R_{ij} = K_{left}^{-1} H_{ij} K_{left}$. In practice due to errors in the computed H_{ij}, the above matrix will not be orthonormal. So for the estimation of R_{ij} [45], an iterative minimization procedure will be applied to: $\sum_k dist(p'_k, K_{left} R_{ij} K_{left}^{-1} p_k)^2$, where (p_k, p'_k) are the inlier matches that resulted after estimation of H_{ij} while $dist$ denotes euclidean image distance. The projection of $K_{left}^{-1} H_{ij} K_{left}$ to the space $SO(3)$ of 3D rotation matrices will be given as initial value to the iterative procedure.

B. Geometric rectification of local models

Since at this stage the rotation between any two local models is known, hereafter we may assume that the 3D vertices of all L_i are expressed in a common 3D coordinate system. Unfortunately L_i are not geometrically consistent with each other, so the model resulting from combining these local models directly, would contain a lot of discontinuities at the boundary between any 2 neighboring L_i (see Fig. 16(c)). This is true because L_i have been created independently and their geometry has been estimated only approximately.

Let $\mathrm{RECTIFY}_{L_i}(L_j)$ denote an operator which takes as input 2 local models, L_i, L_j, and modifies the geometric-maps only of the latter so that they are consistent with the geometric-maps of the former (the geometric maps of L_i do not change during RECTIFY). Assuming that such an operator exists , then ensuring consistency between all models can be achieved by merely applying $\mathrm{RECTIFY}_{L_i}(L_j)$ for all pairs L_i,L_j with $i < j$.

So it suffices that we define $\mathrm{RECTIFY}_{L_i}(L_j)$ for any 2 models, say L_i, L_j. Let X, Y, Z be the new rectified geometric-maps of L_j that we want to estimate so that they are geometrically consistent with those of L_i. Since we know homography H_{ij}, we may assume that image points of L_i have been aligned to the image plane of L_j. Let $\Psi = dom_i \cap dom_j$ be the overlap region of the 2 models. To be geometrically consistent, the new rectified maps of L_j should coincide with those of L_i at points inside Ψ:

$$\Big[X(p)\ Y(p)\ Z(p)\Big] = \Big[X_i(p)\ Y_i(p)\ Z_i(p)\Big]\ ,\ \forall p \in \Psi \tag{12}$$

We still need to define the rectified maps on $\bar{\Psi} = dom_j \backslash \Psi$ (i.e. the complement of Ψ in dom_j). On one hand, this must be done so that no discontinuity appears along $\partial\bar{\Psi}$ (and thus seamless rectified maps are produced). On the other hand, we must try to preserve the relative 3D structure of the existing geometric-maps (of L_j) in the interior of $\bar{\Psi}$. The last statement amounts to:

$$\begin{bmatrix} X(p)-X(q) \\ Y(p)-Y(q) \\ Z(p)-Z(q) \end{bmatrix} = \begin{bmatrix} X_j(p)-X_j(q) \\ Y_j(p)-Y_j(q) \\ Z_j(p)-Z_j(q) \end{bmatrix} \quad \forall p, q \in \bar{\Psi}$$

or equivalently:

$$\begin{bmatrix} \nabla X(p) \\ \nabla Y(p) \\ \nabla Z(p) \end{bmatrix} = \begin{bmatrix} \nabla X_j(p) \\ \nabla Y_j(p) \\ \nabla Z_j(p) \end{bmatrix}\ ,\ \forall p \in \bar{\Psi} \tag{13}$$

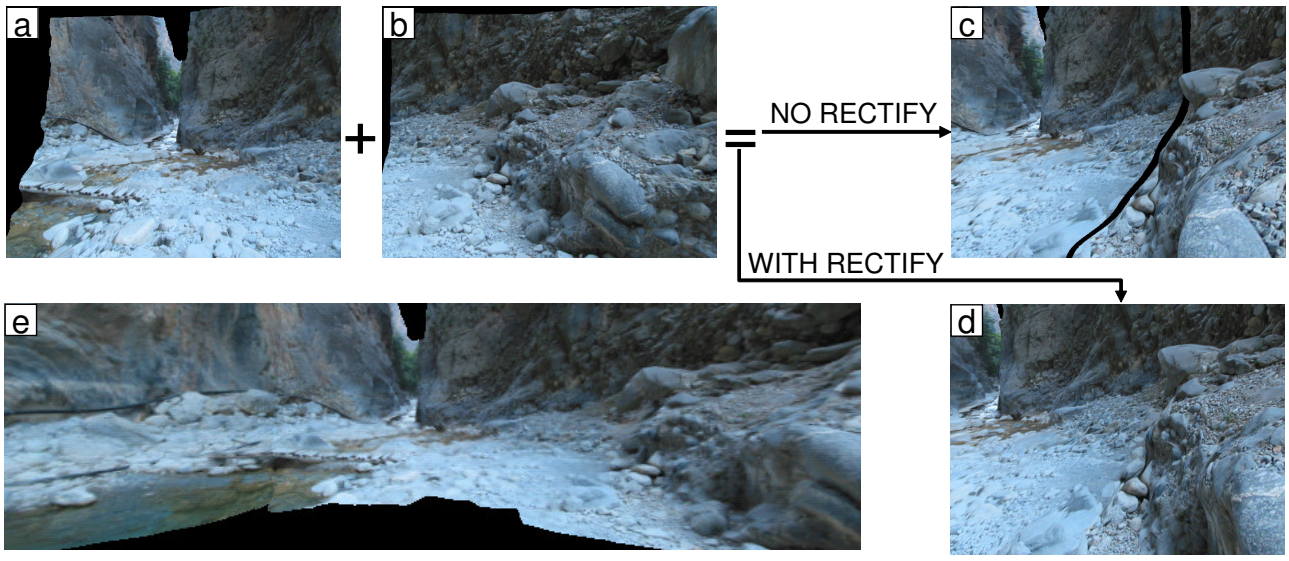

Fig. 16: Rendered views of: **(a)** a local model L_j **(b)** a local model L_i **(c)** a 3D-mosaic of L_i, L_j without geometry rectification (holes are due to errors in the geometry of the local models and not due to misregistration in 3D space) **(d)** a 3D-mosaic of L_i, L_j after $\mathrm{RECTIFY}_{L_i}(L_j)$ has been applied **(e)** a bigger 3D-mosaic created from L_i, L_j as well as another local model which is not shown

Then, based on (13), (12), we can extract the Z rectified map (X, Y maps are treated analogously) by solving the following optimization problem:

$$\min_{Z} \iint_{\bar{\Psi}} \|\nabla Z - \nabla Z_j\|^2, \;\; Z|_{\partial\bar{\Psi}} = Z_i|_{\partial\bar{\Psi}} \tag{14}$$

The above problem, like the one defined by (7), can be reduced either to a banded linear system or to a Poisson differential equation, as explained in section VI-B. See Fig. 16(d) for a result produced with the latter method.

Another option for the merging of the geometric maps of L_i, L_j could have been the use of a feathering-like approach. The advantage of our approach (against feathering) is the preservation of the model's 3D structure. This can be illustrated with a very simple example (see Figure 17). Let a rectangular planar object be at constant depth Z_{true}. Suppose that depth map Z_i, corresponding to most of the left part of the object, has been estimated correctly ($Z_i \equiv Z_{true}$) but depth map Z_j, corresponding to most of the right part of the object, has been estimated as $Z_j \equiv Z_{true} + error$. When using a feathering-like approach, the resulting 3D object will appear distorted in the center (its depth will vary from Z_{true} to $Z_{true} + error$ therein) and this distortion will be very annoying to the eye. On the contrary, by using our method, a 3D object still having a planar structure will be produced. This is important since such errors often exist in models produced from disparity estimation. In fact, in this case, the errors' magnitude will be proportional to depth and can thus be quite large for distant (to the camera) objects, such as local models of large scale scenes.

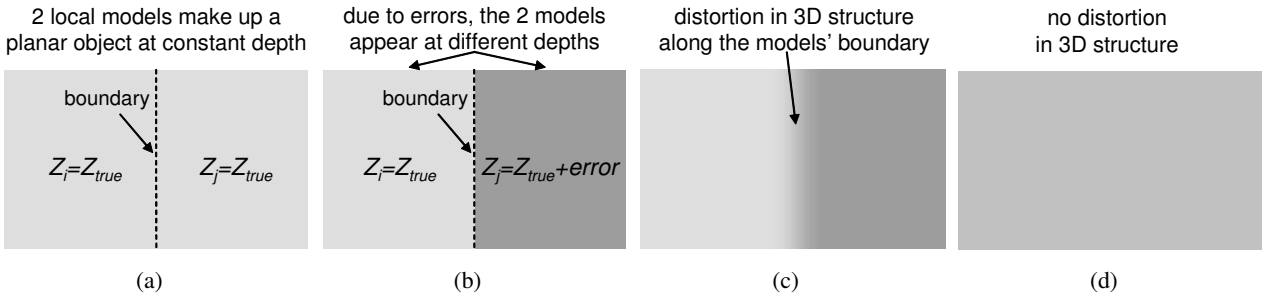

Fig. 17: A synthetic example illustrating the superiority of our approach against feathering (see also text). **(a)** True depth maps. **(b)** Estimated noisy depth maps. **(c)** Resulting 3D-mosaic's depth map using feathering. **(d)** Resulting 3D-mosaic's depth map using our method.

C. Merging the rectified local models

Since H_{ij} is known for any i, j, we may assume that all local models are defined on a common image plane. Therefore, due to the fact that the rectified geometric-maps are consistent with each other, we can directly merge them so that the $\{X, Y, Z\}_{mosaic}$ maps are produced. For the creation of the I_{mosaic} photometric map, a standard image-mosaicing procedure [45] can be applied independently. The valid region of the 3D-mosaic will be: $dom_{mosaic} = \cup_i dom_i$. Two 3D-mosaics that have been constructed in this manner appear in Figures 16(e) and 18.

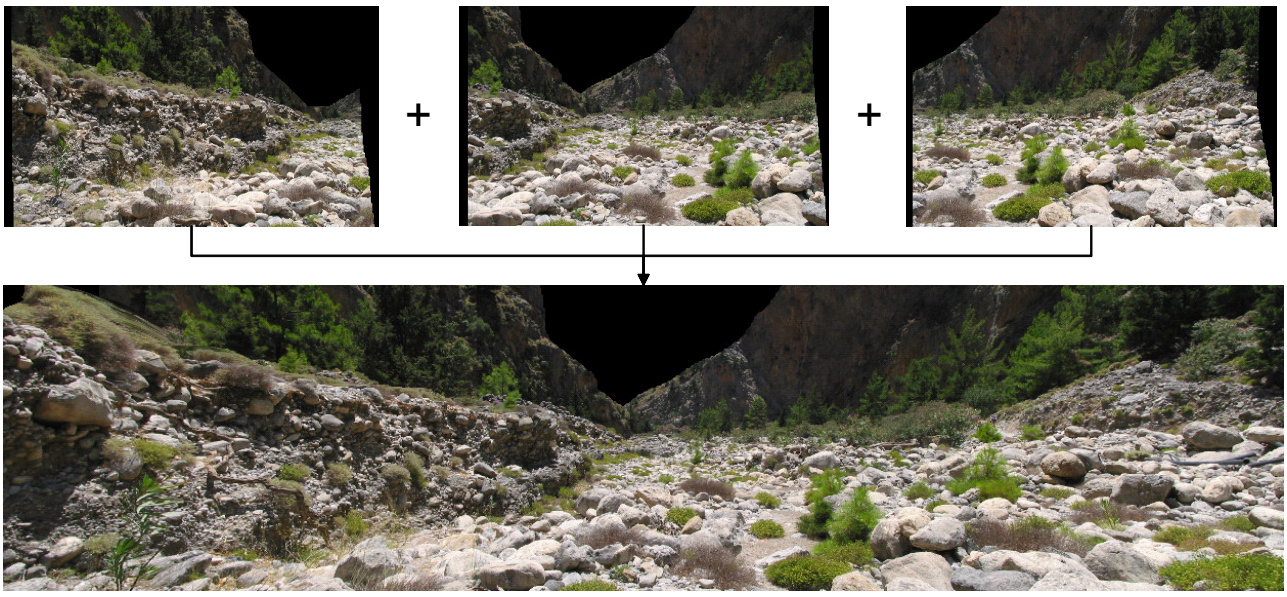

Fig. 18: Another example of a 3D-mosaic constructed using our method. **Top row:** three separate local 3D-models **Bottom row:** the resulting 3D-mosaic

IX. Further results

As part of a research project, the "morphable 3D-mosaic" framework has been already successfully applied to the visual 3D reconstruction of the well known Samaria Gorge in Crete (a gorge which is considered to be one of the most magnificent in the world and which was also awarded by the Council of Europe with a Diploma First Class, as being one of Europe's most beautiful spots). Based on this 3D reconstruction, and by also using a 3D Virtual Reality installation, the ultimate goal of that work has been to provide a lifelike virtual tour of the Samaria Gorge to all visitors of the National History Museum of Crete, located in the city of Heraklion. To this end, the most beautiful spots along the gorge have been selected and for each such spot a predefined path, that was over 100 meters long, was chosen as well. About 15 key-positions have been selected along each path and approximately 45 stereoscopic views have been acquired at these positions with 3 stereoscopic views corresponding to each position (this way a 120^{o} wide field of view has been covered). Using the reconstructed "morphable 3D-mosaics", a photorealistic walkthrough of the Samaria Gorge has been obtained, which was visualized at interactive frame rates by means of a virtual reality system. The hardware equipment that has been used for the virtual reality system was a PC (with a Pentium 4 2,4GHz CPU on it) which was connected to a single-channel stereoscopic projection system from Barco consisting of a pair of circular polarized LCD projectors (Barco Gemini), an active-to-passive stereo converter as well as a projection screen. The rendering was done on a GeForce 6800 3D graphics card (installed on the PC) and, for the stereoscopic effect to take place, 2 views (corresponding to the left and right eye) were rendered by the graphics card at

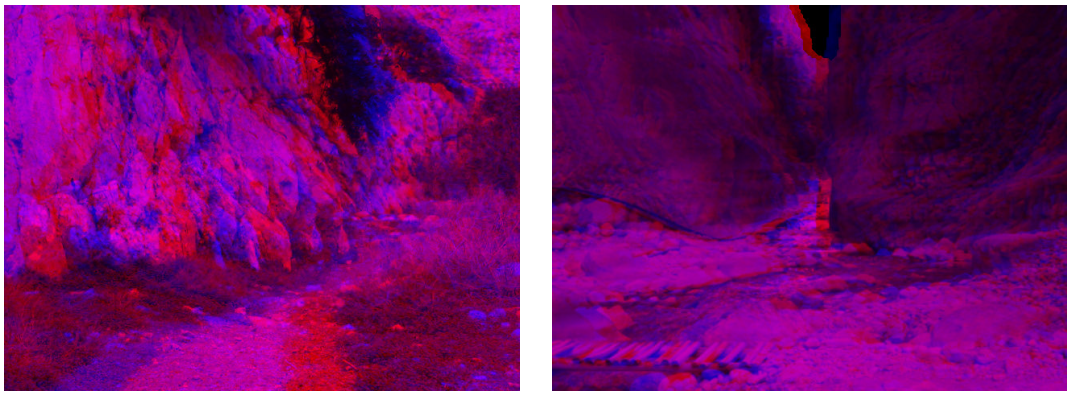

(a) (b)

Fig. 19: Two stereoscopic views as would be rendered by the VR system (for illustration purposes these are shown in the form of red-blue images).

(a) Sample views of a morphable 3D model. Each view corresponds to a different amount of morphing.

(b) Sample views (each with a different amount of morphing) for another morphable 3D model.

Fig. 20: Each row contains sample renderings that were produced using just one morphable 3D model. The leftmost, rightmost images in each row correspond to the renderings at positions pos_k, pos_{k+1} respectively.

any time. Museum visitors were then able to participate in the virtual tour simply by wearing stereo glasses that were matched to the circular polarization of the projectors. Two sample stereoscopic views, as would be rendered by the VR hardware, are shown in Figure 19. Despite the fact that a single graphics card has been used, very high frame rates of about 25fps in stereo mode (i.e. 50fps in mono mode) were obtained thanks to the optimized rendering pipeline provided by our framework. A sample from the obtained rendering results (that were generated in real time) are shown in Figure 20 for two different morphable models. In each row of that figure the leftmost and rightmost images represent rendered views of the model L_k and L_{k+1} respectively, while the images in between represent intermediate views of the morphable model along the path. Also, in Figure 21, we show some more rendered views where, this time, the virtual camera traverses a path containing more than one morphable 3D model. A corresponding video, containing only a short clip from a virtual tour into the Samaria Gorge, is also available at the following URL: `http://www.csd.uoc.gr/~komod/research/morphable_3d_mosaics/`.

Another difficulty that we had to face, during the visual reconstruction of the Samaria Gorge, was related to the fact that a small river was passing through a certain part of the gorge. This was a problem for the construction of the local 3D models as our stereo matching algorithm could not possibly extract disparity (i.e. find correspondences) for the points on the water surface. This was so because the water was moving and, even in places where it was static, sun reflections that existed on its surface were violating the lambertian assumption during stereo matching (see Figure 22(a)). Therefore, the disparity for all pixels lying on the water had to be estimated in a different way.

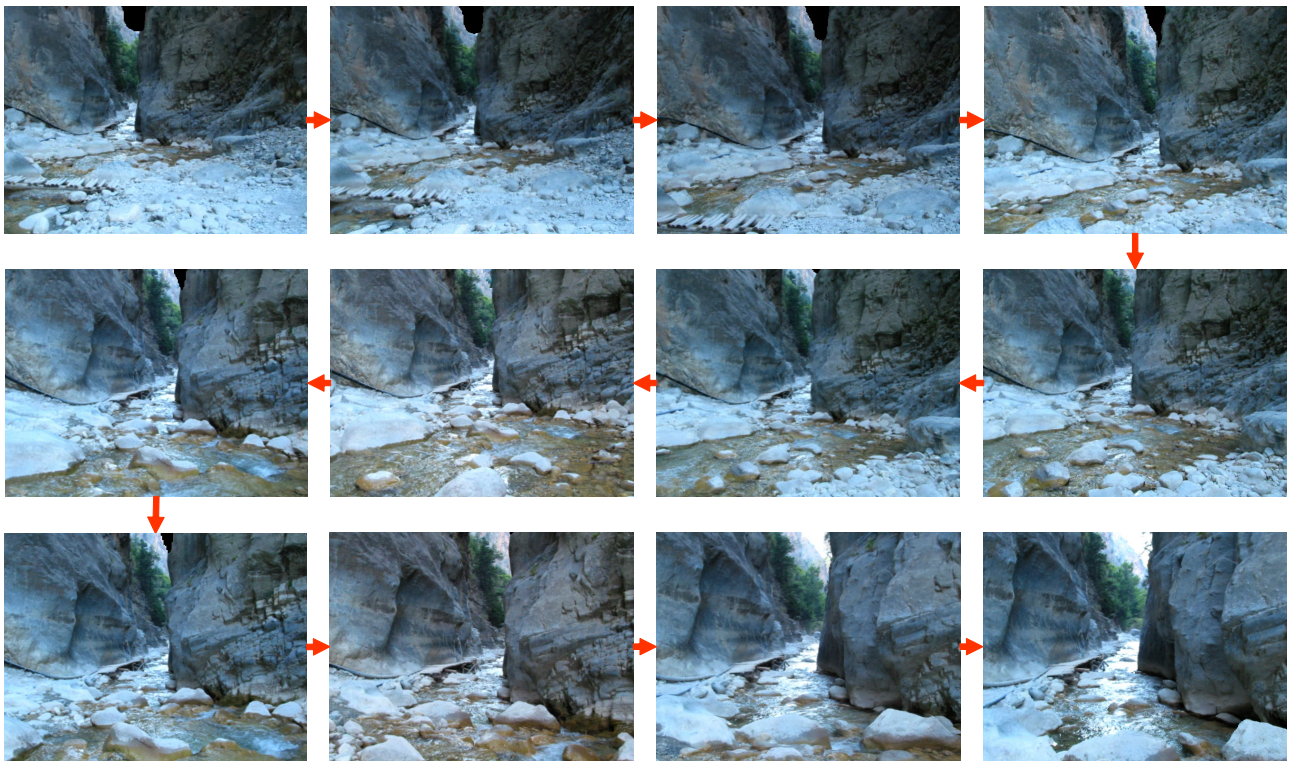

Fig. 21: Some rendered views that are produced as the virtual camera traverses a path through the so-called "Iron Gates" area, which is the most famous part of the Samaria Gorge. In this case, the virtual camera passes through multiple morphable 3D models.

To this end, as the water surface was approximately planar, a 2D homography (i.e. a 2D projective transformation represented by a 3×3 homogeneous matrix H_{water}), directly mapping left-image pixels on the water to their corresponding points in the right image, was estimated. For estimating H_{water}, we made use of the fact that most left-image pixels that are located on the ground next to the river lie approximately at the same plane as the water surface and, in addition to that, stereo matching can extract valid correspondences for these pixels, as they are not on the water. A set $\{g_i\}_{i=1}^{K}$ of such pixels in the left image is thus extracted and their matching points $\{g'_i\}_{i=1}^{K}$ in the right image are also computed based on the already estimated disparity maps. The elements of H_{water} can then be easily recovered by minimizing, through a robust procedure like RANSAC, the total reprojection error i.e. the sum of distances between $\{H_{water} \cdot g_i\}_{i=1}^{K}$ and $\{g'_i\}_{i=1}^{K}$. An example of a disparity field that has been estimated with this method can be seen in Figure 22(c). We should note that, by using a similar method, a 2D homography $H_{water}^{k \rightarrow k+1}$, mapping pixels of I_k lying on the water to their corresponding pixels in image I_{k+1}, can be computed as well. This way we can also manage to estimate optical flow $u_{k \rightarrow k+1}$ for all pixels of image I_k including those pixels of I_k

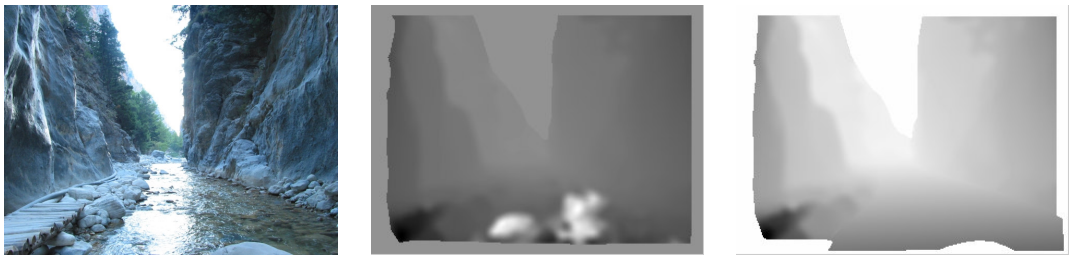

(a) (b) (c)

Fig. 22: (a) The left image of a stereoscopic image pair that has been captured at a region passing through a small river. **(b)** The estimated disparity by using a stereo matching procedure. As expected, the disparity field contains a lot of errors for many of the points on the water surface. This is true especially for those points that lie near the sun reflections on the water. **(c)** The corresponding disparity when a 2D homography is being used to fill the left-right correspondences for the points on the water. In this case the water surface is implicitly approximated by a 3D plane.

that lie on the water.

Finally, we should mention that one of the additional benefits of having a virtual 3D reconstruction of the gorge is the ability e.g. to add synthetic visual effects or integrate synthetic objects into the environment. This way the visual experience of a virtual tour inside the gorge can be enhanced even further. For example, in Figure 23(a), we are showing some rendered views of the gorge where we have also added synthetically generated volumetric fog while, in Figures 23(b) and 23(c), we show a synthetic view where an *agrimi* (a wild goat which can be found only in the area of the Samaria Gorge) as well as an oleander plant has been integrated into the 3D virtual environment.

X. Conclusions

In conclusion, we have presented a new approach for obtaining photorealistic and interactive walkthroughs of large, outdoor scenes. To this end a new hybrid data structure has been presented which is called "morphable 3D-mosaics". No global model of the scene needs to be constructed and at any time during the rendering process, only one "morphable 3D-mosaic" is displayed. This enhances the scalability of the method to large environments. In addition, the proposed method uses a rendering path which is highly optimized in modern 3D graphics hardware and thus can produce photorealistic renderings at interactive frame rates. In the future, we intend to extend our rendering pipeline so that it can also take into account data from sparse stereoscopic views that have been captured at locations throughout the scene and not just along a predefined path. This could further enhance the quality of the rendered scene and would also permit a more extensive exploration of the virtual environment. Moreover, this extension still fits perfectly to the current architecture of our 3D-accelerated rendering pipeline (a blending of multiple local models will still

(a)

(b) (c)

Fig. 23: (a) Some rendered views of the gorge that also contain a synthetically generated volumetric fog. **(b)** A rendered view where a synthetic 3D model of the *agrimi*, a wild animal which is specific to the Samaria Gorge, has been integrated into the 3D virtual environment. **(c)** Another view with an oleander plant integrated as well.

be taking place), and so our system can be very easily modified to accommodate this extension. Furthermore, we intend to eliminate the need for a calibration of the stereoscopic camera as well as to allow the stereo baseline to vary during the acquisition of the various stereoscopic views (this will make the data acquisition process even easier). Another issue that we want to investigate is the ability of capturing the dynamic appearance of any moving objects such as moving water or grass that are frequently encountered in outdoor scenes (instead of just rendering these objects as static). To this end we plan to enhance our "morphable 3D-mosaic" framework so that it can also make use of real video textures that have been previously captured inside the scene. One limitation of our method is that it currently assumes that the lighting conditions across the scene are not drastically different (something which is not always true in outdoor environments). One possible approach, for dealing with this issue, is to obtain the radiometric response function of each photograph as well.

REFERENCES

[1] R. Hartley and A. Zisserman, *Multiple View Geometry in Computer Vision*. Cambridge, 2000.

[2] O. Faugeras, Q.-T. Luong, and T. Papadopoulo, *The Geometry of Multiple Images : The Laws That Govern the Formation of Multiple Images of a Scene and Some of Their Applications*. MIT Press, 2001.

[3] Y. Ma, S. Soatto, J. Kosecka, and S. Sastry, *An Invitation to 3D Vision*. Springer, 2005.

[4] L. McMillan, "An image-based approach to three-dimensional computer graphics," Ph.D. dissertation, University of North Carolina, Apr 1997.

[5] E. H. Adelson and J. R. Bergen, "The plenoptic function and the elements of early vision," in *Computational Models of Visual Processing*. Cambridge, MA: MIT Press, 1991, pp. 3–20.

[6] N. Komodakis, G. Pagonis, and G. Tziritas, "Interactive walkthroughs using morphable 3d-mosaics," in *Proc.of the second International Symposium on 3DPVT (3DPVT 2004)*, 2004.

[7] N. Komodakis and G. Tziritas, "Morphable 3d-mosaics: a framework for the visual reconstruction of large natural scenes," *to appear in the video proceedings of CVPR 2006*.

[8] S. Teller, "Automated urban model acquisition: Project rationale and status," in *Teller, S. (1998). Automated urban model acquisition: Project rationale and status. In Proceedings of the Image Understanding Workshop (pp. 455–462). Monterey, CA.*, 1998.

[9] H.-Y. Shum, R. Szeliski, S. Baker, M. Han, and P. Anandan, "Interactive 3d modeling from multiple images using scene regularities." in *SMILE*, 1998, pp. 236–252.

[10] D. Nistér, "Automatic passive recovery of 3d from images and video." in *3DPVT*, 2004, pp. 438–445.

[11] R. Koch, "3d surface reconstruction from stereoscopic image sequences," in *Proc. of the IEEE Int. Conf. on Computer Vision (ICCV 1995)*, 1995, pp. 109–114.

[12] M. Pollefeys, L. J. V. Gool, M. Vergauwen, F. Verbiest, K. Cornelis, J. Tops, and R. Koch, "Visual modeling with a hand-held camera." *International Journal of Computer Vision*, vol. 59, no. 3, pp. 207–232, 2004.

[13] C. Strecha, R. Fransens, and L. J. V. Gool, "Wide-baseline stereo from multiple views: A probabilistic account." in *CVPR (1)*, 2004, pp. 552–559.

[14] C. Strecha and L. J. V. Gool, "Pde-based multi-view depth estimation." in *3DPVT*, 2002, pp. 416–427.

[15] C. Strecha, T. Tuytelaars, and L. J. V. Gool, "Dense matching of multiple wide-baseline views." in *ICCV*, 2003, pp. 1194–1201.

[16] P. E. Debevec, C. J. Taylor, and J. Malik, "Modeling and rendering architecture from photographs: A hybrid geometry- and image-based approach," in *SIGGRAPH 96*, 1996, pp. 11–20.

[17] S. Fleishman, B. Chen, A. Kaufman, and D. Cohen-Or, "Navigating through sparse views," in *VRST99*, pp. 82-87, 1999.

[18] L. McMillan and G. Bishop, "Plenoptic modeling: An image-based rendering approach," in *SIGGRAPH95*, pp. 39-46, 1995.

[19] M. Levoy and P. Hanrahan, "Light field rendering," in *SIGGRAPH 96*, 1996, pp. 31–42.

[20] S. Gortler, R. Grzeszczuk, R. Szeliski, and M. Cohen, "The lumigraph," in *SIGGRAPH 96*, 1996, pp. 43–54.

[21] C. Buehler, M. Bosse, L. McMillan, S. J. Gortler, and M. F. Cohen, "Unstructured lumigraph rendering." in *Proc. of SIGGRAPH 2001*, 2001, pp. 425–432.

[22] H. Schirmacher, M. Li, and H.-P. Seidel, "On-the-fly processing of generalized Lumigraphs," in *Proc. of Eurographics 2001*, vol. 20, no. 3, 2001, pp. C165–C173;C543.

[23] S. Vedula, S. Baker, and T. Kanade, "Spatio-temporal view interpolation," in *Proceedings of the 13th ACM Eurographics Workshop on Rendering*, June 2002.

[24] W. Matusik, C. Buehler, R. Raskar, S. J. Gortler, and L. McMillan, "Image-based visual hulls," in *Proc. of SIGGRAPH 2000*, 2000, pp. 369–374.

[25] C. L. Zitnick, S. B. Kang, M. Uyttendaele, S. Winder, and R. Szeliski, "High-quality video view interpolation using a layered representation," *ACM Trans. Graph.*, vol. 23, no. 3, pp. 600–608, 2004.

[26] M. Uyttendaele, A. Criminisi, S. B. Kang, S. Winder, R. Hartley, and R. Szeliski, "High-quality image-based interactive exploration of real-world environments," *IEEE Computer Graphics & Applications*, 2004.

[27] D. G. Aliaga, T. Funkhouser, D. Yanovsky, and I. Carlbom, "Sea of images," in *VIS 2002*, 2002, pp. 331–338.

[28] J.-Y. Bouguet, "Camera Calibration Toolbox for MATLAB," http://www.vision.caltech.edu/bouguetj/calib_doc.

[29] I. Grinias and G. Tziritas, "Robust pan, tilt and zoom estimation." in *Intern. Conference on Digital Signal Processing*, 2002.

[30] J. Barron, D. Fleet, and S. Beauchemin, "Performance of optical flow techniques," *International Journal of Computer Vision*, vol. 12, pp. 43–77, 1994.

[31] M. J. Black and P. Anandan, "The robust estimation of multiple motions: Parametric and piecewise-smooth flow fields," *CVIU*, vol. 63, no. 1, pp. 75–104, 1996.

[32] N. Komodakis and G. Tziritas, "A new framework for approximate labeling via graph-cuts." in *ICCV*, 2005, pp. 1018–1025.

[33] S. Coorg and S. Teller, "Spherical mosaics with quaternions and dense correlation," *Int. J. Comput. Vision*, vol. 37, no. 3, pp. 259–273, 2000.

[34] B. K. P. Horn, "Closed form solution of absolute orientation using unit quaternions," *Journal of The Optical Society of America A*, vol. 4, no. 4, April 1987.

[35] T. Tuytelaars and L. V. Gool, "Wide Baseline Stereo Matching based on Local, Affinely Invariant Regions," in *Proceedings of British Machine Vision Conference*, 2000, pp. 412–422.

[36] K. Mikolajczyk and C. Schmid, "An affine invariant interest point detector," in *ECCV (1)*, 2002, pp. 128–142.

[37] D. G. Lowe, "Distinctive image features from scale-invariant keypoints," *Int. J. Comput. Vision*, vol. 60, no. 2, pp. 91–110, 2004.

[38] S. Li, *Markov Random Field Modeling in Computer Vision*. Springer-Verlag, 1995.

[39] P. F. Felzenszwalb and D. P. Huttenlocher, "Efficient belief propagation for early vision." in *CVPR*, 2004, pp. 261–268.

[40] Y. Boykov, O. Veksler, and R. Zabih, "Fast approximate energy minimization via graph cuts," *IEEE Transactions on Pattern Analysis and Machine Intelligence*, vol. 23, no. 11, pp. 1222–1239, November 2001.

[41] D. Zwilliger, *Handbook of Differential Equations*. Boston, MA: Academic Press, 1997.

[42] P. Perez, M. Gangnet, and A. Blake, "Poisson image editing," *ACM Trans. Graph.*, vol. 22, no. 3, pp. 313–318, 2003.

[43] M. Segal and K. Akeley, "The OpenGL Graphics System: A Specification (Version 1.5)," http://www.opengl.org.

[44] P. S. Heckbert and M. Garland, "Survey of polygonal surface simplification algorithms," *in SIGGRAPH 97 course notes on multiresolution surface modeling*.

[45] R. Szeliski, "Video mosaics for virtual environments," *IEEE Computer Graphics and Applications*, vol. 16, no. 2, pp. 22–30, March 1996.